Solid State Nuclear Magnetic Resonance xxx (xxxx) 101973

Contents lists available at ScienceDirect

Solid State Nuclear Magnetic Resonance

journal homepage: www.elsevier.com/locate/ysnmr

Glucose hydrochar consists of linked phenol, furan, arene, alkyl, and ketone structures revealed by advanced solid-state nuclear magnetic resonance

Shichen Yuan [a, 1], Avery Brown [b, 1], Zhaoxi Zheng [a], Robert L. Johnson [c], Karen Agro [b], Andrea Kruse [d], Michael T. Timko [b], Klaus Schmidt-Rohr [a, *]

[a] Brandeis University, Department of Chemistry, Waltham, MA, 02453, USA
[b] Worcester Polytechnic Institute, Department of Chemical Engineering, 100 Institute Road, Worcester MA, 01609, USA
[c] Hawai'i Natural Energy Institute, University of Hawai'i at Manoa, Honolulu, HI 96822, USA
[d] University of Hohenheim, Institute of Agricultural Engineering, Department of Conversion Technologies of Biobased Resources, Garbenstrasse 9, 70599, Stuttgart, Germany

ARTICLE INFO

Handling Editor: Prof D Bryce

Keywords:
Hydrochar structure
Hydrothermal carbon
Quantitative solid-state ^{13}C NMR
Spectral editing
Hydroxyl-proton selection
Catechols
Diphenols
Hydrochar models

ABSTRACT

The molecular structure of hydrochars produced from ^{13}C-enriched glucose under various conditions has been elucidated based on advanced one- and two-dimensional (2D) ^{1}H-^{13}C and ^{13}C–^{13}C solid-state nuclear magnetic resonance (NMR) with spectral editing. Regardless of synthesis conditions, hydrochars consist mostly of oxygen-substituted arene rings (including diphenols) and furans connected by alkyl linkers rich in ketones. Cross-linking nonprotonated and methyne (C-H) alkyl carbons have been identified through spectrally edited 2D NMR. Alkenes and 'quaternary' C-O are observed only at low synthesis temperature, while some clusters of fused arene rings are generated at high temperature. Hydrochar composition is nearly independent of reaction time in the range from 1 to 5 h. Equilibration of ^{13}C magnetization within 1 s shows that the materials are homogeneous on the 5-nm scale, refuting core–shell models of hydrochar microspheres. While furan C-O carbons bonded to alkyl groups or ketones show distinctive cross peaks in 2D NMR, phenolic C-OH is observed unambiguously by hydroxyl-proton selection. While methylene-linked furan rings are fairly common, the signal previously assigned to furan Cα-Cα linkages is shown to arise from abundant, stable catecholic *ortho*-diphenols, whose HO-C = C-OH structure is proved by 2D^{13}C–^{13}C NMR after hydroxyl-proton selection. Quantitative ^{13}C NMR spectra of low- and high-temperature hydrochars have been matched by chemical-shift simulations for representative structural models. Mixed phenol and furan rings connected by ketones and alkyl linkers provide good fits of the experimental spectra, while literature models dominated by large clusters of fused rings and with few phenols or alkyl-linked ketones do not.

1. Introduction

Amorphous carbon-rich materials are useful for numerous purposes, including gas separation and storage, pollution remediation, anodes for lithium-ion batteries, supercapacitors, sensors [1], and biomedical applications [2]. For applications in catalysis of water-soluble biomolecules, good resistance to degradation in hot aqueous conditions makes carbon materials superior to hydrothermally unstable oxide catalysts [3–5]. Advanced carbonaceous materials can be produced from renewable feedstocks by the process of hydrothermal carbonization (HTC), which has attracted significant research interest [6] as an industrially viable process that is energy-neutral due to its exothermic nature. The resulting hydrothermal chars (hydrochar) exhibit favorable chemical and morphological properties, which can be modified and tuned by the incorporation of metal catalyst or by altering the duration [7], acidity, or temperature [8] of the hydrothermal conversion process [5,6]. Hydrothermal carbonization of carbohydrates produces carbon-rich spheres of fairly uniform diameter between 50 and 1000 nm, depending on reaction conditions [9,10]. Importantly, the structure of hydrochar appears to depend minimally on the carbohydrate precursor materials used, and it has been established that materials produced from glucose are similar to those from biomass [11].

The formation of solid hydrochar spheres [9,10] has been explained in terms of a two-step mechanism. First, the solid biomass hydrolyzes to form soluble sugar monomers and short oligomers; next, these dissolved species undergo dehydration and condensation reactions that co-

* Corresponding author. Department of Chemistry, Brandeis University, 415 South Street, Waltham, MA, 02453, USA.
E-mail address: srohr@brandeis.edu (K. Schmidt-Rohr).
[1] These authors contributed equally to this work.

https://doi.org/10.1016/j.ssnmr.2024.101973
Received 4 August 2024; Received in revised form 9 October 2024; Accepted 9 October 2024
0926-2040/

alesce to form solid carbon spheres. Hydrochar synthesis affords the opportunity to incorporate a wide variety of heteroatoms, functional groups, nanoparticles, and quantum dots during the synthesis to produce an array of nanocomposite materials with tunable catalytic, electrochemical, and magnetic properties [12–15].

For the rational development of hydrochar materials targeted for specific applications, an understanding of their chemical and nanometer-scale structure is crucial. Given the amorphous nature of the materials, diffraction techniques provide rather limited information [10,16,17]. As a result of the relatively low synthesis temperature, these materials contain significant fractions of oxygen and hydrogen and therefore have a broad distribution of functional groups that produce poorly resolved patterns in unselective vibrational or magnetic-resonance spectra. Thermally programmed desorption (TPD) monitors the evolution of CO and CO_2 in order to indirectly identify various oxygen-containing groups [18], but deconvolution of the observed peaks is rather ambiguous with materials synthesized at low temperature (such as hydrochar), as further reactions may occur prior to the release of gases. X-ray photoelectron spectroscopy (XPS) can be used for the analysis of the chemical composition, types of bonding, and their proportions in amorphous carbon materials [19]. However, it suffers from strong peak overlap [20] and contamination by environmental gases [21], which has limited its usefulness in application to hydrochar. Near-edge X-ray absorption fine structure (NEXAFS) can distinguish only a handful of structural units, does not provide intrinsic quantification, and cannot probe the bulk of the material [16]. Raman spectroscopy is sensitive to the short- and medium-range atom ordering in amorphous carbon materials [22], but hydrochar is subject to thermal degradation during analysis [23] and the resulting Raman spectra consist of only a handful of broad features that are not easily deconvolved [24]. Careful utilization of Raman spectroscopy without laser-induced pyrolysis has led to the successful characterization of local structures in many hydrothermal carbonizations [23,24], especially for the quantification of furan/arene type ring structures and fused aromatic rings yet leaves many questions unanswered including the nature of linking groups.

The aforementioned technical challenges have not completely discouraged attempts to rationalize the molecular structure of hydrochar. An early chemical model depicted hydrochar as consisting of large arene clusters with heteroatoms on their peripheries, based on Raman spectroscopic analysis of materials synthesized at ≥350 °C [10,25]. However, large arene clusters are not representative of hydrochars commonly prepared at lower temperatures, as shown by Baccile et al. [26] using solid-state ^{13}C nuclear magnetic resonance (NMR) with ^{13}C-enriched starting materials. Based on spectra from two-dimensional (2D) double-quantum correlation experiments, they proposed instead that hydrochar spheres are primarily composed of directly linked furan rings as well as minor fractions of short alkyl linkers with ketones, aldehyde groups and significant amounts of immobilized levulinic acid. These oxygen-rich structures are believed to result from a mechanism that proceeds through the dehydration of glucose to hydroxymethylfurfural (HMF), which further dehydrates intermolecularly and condenses into insoluble clusters that agglomerate into spheres. Arenes were estimated to account for about 10 % of the material and proposed to form separate domains consisting of aromatic clusters of about seven fused rings [26].

Earlier spectroscopic studies of hydrochar composition did not have the sophistication required to elucidate the structural complexity of hydrochar, such as coexisting furans and phenols, aromatic rings and alkenes, or ketones and aldehydes, whose NMR signals overlap. As a result, in hindsight some of their conclusions, for instance regarding the absence of phenols, have turned out to be too simplistic. Of the existing models, those proposed from NMR spectra are the most comprehensive, yet they too lack key details.

Here we probe the structure of a suite of ^{13}C-enriched hydrochars by more advanced NMR techniques including spectral editing [27–31] combined with two-dimensional spectroscopy, which can resolve crucial overlapping signals. Our new structural insights are based on experiments taking advantage of one- and two-bond ^{1}H-^{13}C dipolar couplings as well as multiple-bond ^{13}C–^{13}C interactions, which were not utilized in the earlier NMR analysis reported in Ref. [26]. For instance, hydroxyl-proton selection [30] in one- and two-dimensional spectra enables us to distinguish phenols from furans; in particular, *ortho*-diphenols are unequivocally separated from difurans. We can also observe other clear signals of arenes and prove their proximity to ketones and methylenes by means of 2D ^{13}C–^{13}C correlation spectra edited using ^{13}C-^{1}H one-bond couplings [31].

For a quantitative analysis of hydrochar composition, we apply comprehensive structural modeling with chemical-shift prediction to match quantitative ^{13}C NMR spectra [4]. This enables quantification of the composition without simplistic assumptions about chemical-shift ranges of furans and arenes and provides a straightforward way to compare the quality of different structural models, including those proposed in the literature. This approach yields good estimates of the fractions of carbons in furans, phenols, other arenes, alkyls, ketones, and carboxylates.

In addition to molecular-level characterization, hydrochar structure on the length scale of tens of nanometers may be important in some applications. The structure of hydrochar spheres on the ~100-nm scale has been described as a two-domain system composed of a hydrophilic shell surrounding a hydrophobic core [9,10]. This model was derived from electron micrographs that display less intensity in the outer region of each sphere and would be compatible with a reaction mechanism in which the aromatic solid grows by attachment of hydrophilic molecules from solution. We test this hypothesis by two-dimensional ^{13}C–^{13}C exchange NMR experiments with long mixing times, where the extent of ^{13}C spin diffusion gives a good measure of spatial proximities and homogeneity on the 5-nm scale.

Hydrothermal carbon syntheses have been reported for a range of temperatures (typically between 180 and 350 °C) [8], reaction times (0.5–24 h) [7], and pH conditions [6]. These conditions may impact the structure of the resulting hydrochar. To determine the effects of synthesis parameters on structure and to draw structural conclusions that may apply to hydrochars in general, the structures of nine samples synthesized at various temperatures and pH conditions for two different reaction times were characterized by quantitative ^{13}C NMR in this study.

2. Materials and methods

2.1. Sample preparation

^{13}C-enriched D-glucose ($^{13}C_6H_{12}O_6$, >99 % atom % ^{13}C, molecular weight 186.11 g/mol) from Sigma-Aldrich was selected as the source of ^{13}C, while regular alpha-D(+)-glucose ($C_6H_{12}O_6$, molecular weight 180.16 g/mol) was purchased from Fisher Scientific.

Hydrothermal conversions of model solutions of 1.4 g of glucose in deionized water (>17.9 MΩ resistivity) were conducted with ^{13}C enriched glucose or partially ^{13}C enriched glucose as carbon precursors. Here, "fully-enriched" refers to the carbon source being neat ^{13}C-enriched glucose, while "partially-enriched" refers to a mass ratio of 0.28 g: 1.12 g = 1:4 for ^{13}C-enriched glucose to natural-abundance glucose. The reaction time was either 1 h or 5 h, encoded as "-1h" and "-5h" in the sample nomenclature. The three reaction temperatures tested were 180 °C, 200 °C, and 280 °C (−180, −200, and −280 in the sample name).

The molar ratio of HCl (from a 37 mol% solution (Fisher)) to glucose varied; three levels of HCl concentration were used: 0 M (no acid, NA), 0.016 M (low acid, LA), and 0.16 M (high acid, HA). The abbreviated names, such as ^{13}CGlc-1h-180-HA, of the nine samples studied can be found in Table 1. An overview of the reaction conditions is given in Table S1.

Table 1
Composition of the nine glucose hydrochar materials studied here from peak integration in quantitative ^{13}C NMR spectra and spectral editing. Spinning sidebands were taken into account. In each row, the percentages not in italic font add to 100 ± 1 %. Maximum values in each column are highlighted in bold. Error margins: ±0.6 % for integrals ≤10 %; ±1 % for integrals >10 %.

	Ketone	COO	Arom.	*Arom C_{np}*	OCH_n	*OC_q + CC_q*	CCH_n	*CH_3*
Sample//ppm	230–187	187–164	164–97	*164–97*	97–63	*97–38*	63–8	*34–8*
Glc-1h-**180**-LA	8.6 %	**5.7 %**	56.1 %	*39.5 %*	**6.8 %**	***4.7 %***	22.8 %	*5.5 %*
^{13}CGlc-1h-180-HA	**9.2 %**	5.6 %	54.8 %	*39.6 %*	5.2 %	*4.7 %*	25.2 %	***7.5 %***
Glc-1h-**200**-NA	7.6 %	5.0 %	58.2 %	*40.5 %*	6.7 %	*4.5 %*	22.3 %	*4.9 %*
Glc-5h-200-NA	7.8 %	4.9 %	59.2 %	*43.3 %*	4.8 %	*4.1 %*	23.4 %	*5.7 %*
Glc-1h-200-LA	7.4 %	4.8 %	58.5 %	*44.4 %*	4.2 %	*4.0 %*	25.2 %	*6.5 %*
Glc-5h-200-LA	7.9 %	5.1 %	57.4 %	*42.4 %*	3.6 %	*4.1 %*	25.9 %	*6.4 %*
Glc-1h-200-HA	8.2 %	5.1 %	55.7 %	*40.1 %*	4.7 %	*4.3 %*	**26.3 %**	*6.7 %*
Glc-1h-**280**-NA	6.3 %	3.9 %	63.1 %	*47.0 %*	3.9 %	*3.8 %*	22.7 %	*6.5 %*
^{13}CGlc-5h-280-NA	5.3 %	4.3 %	**64.3 %**	***48.9 %***	3.9 %	*3.3 %*	22.3 %	*7.0 %*

The experiments included hydrothermal conversion of the following model solutions: solution A (S.A, 1.45 M partially-enriched glucose), solution B (S.B, 1.45 M partially-enriched glucose + 0.016 M HCl), solution C (S.C, 1.45 M partially-enriched glucose + 0.16 M HCl), solution D (S.D, 1.45 M fully-enriched glucose), and solution E (S.E, 1.45 M fully-enriched glucose + 0.16 M HCl). The hydrothermal conversion was performed in stainless steel autoclaves with an internal volume of 10 ml. During each experiment, a total of 6 autoclaves were loaded into a thermally insulated gas chromatograph oven. The GC oven temperature was then set to the desired set-point. Each experiment was allowed 40 min to reach the desired set-point after which the reactors were removed after 1 h or 5 h as denoted in Table S1. After the planned reaction time had passed, the autoclave was quenched rapidly by cooling down the autoclave to room temperature in cold water. The reaction conditions of the hydrothermal conversion processes and the corresponding solid samples are summarized in Table S1.

After cooling down the autoclave, the suspension of the solid (hydrochar) and liquid (process water) was filtered using a vacuum pump and a 0.45-μm PTFE membrane filter. Then the hydrochar was dried at 105 °C for 24 h. After drying, the hydrochar was ground via mortar and pestle to produce samples with homogeneously fine particles.

The liquid phase was collected in high-density polyethylene (HDPE) bottles and frozen at −24 °C to avoid oxidation and degradation reactions before characterization using HPLC [32]. The maturity of the solid phase sample was evaluated using the hydrochar yield, residual glucose concentration, concentrations of intermediates such as levulinic acid, and severity factors – as shown in Table S2. Two fully enriched samples were prepared under conditions designed to produce one immature hydrochar and one mature hydrochar.

2.2. Elemental analysis

The C and H mass fractions were measured by combustion analysis at Midwest Microlab, Indianapolis, for ^{13}CGlc-1h-180-HA (62.48 ± 0.3 wt% C, 4.19 ± 0.04 wt% H) and ^{13}CGlc-5h-280-NA (67.72 ± 0.3 wt% C, 4.00 ± 0.04 wt% H).

2.3. Solid-state NMR

NMR experiments were performed on a Bruker Avance Neo 400WB NMR spectrometer at ^{1}H and ^{13}C resonance frequencies of 400 MHz and 100 MHz, respectively. All measurements were conducted using a Bruker double resonance magic-angle-spinning (MAS) probe head with 4-mm zirconia rotors. Samples were directly loaded into the rotors with 3-mm thick glass disks at the bottom, except for the partially labeled Glc-1h-180-LA, which was first loaded into a Kel-F HR-MAS rotor insert due to limited sample amount. The 90° pulse lengths for ^{1}H and ^{13}C were 3.6 μs and 4.0 μs, respectively. Two-pulse phase modulation (TPPM) [33] with strong ^{1}H decoupling at a field strength of $|\gamma B_1/2\pi|$ = 95 kHz was used for dipolar decoupling during the Hahn echo [34] or total suppression of sidebands (TOSS) [35] for dead-time-free detection, while SPINAL-64 [36] at $\gamma B_1/2\pi$ = 85 kHz was used during signal acquisition. ^{13}C chemical shifts were referenced to TMS via the COO resonance of α-1-^{13}C-glycine at 176.49 ppm as a secondary reference.

For each of the nine hydrochar samples studied here, a fully relaxed ^{13}C direct polarization (DP) NMR spectrum with up to 300 s recycle delays (depending on the T_{1C} relaxation time of the sample) was recorded at 14 kHz MAS with signal averaging for up to 13 h.

2.3.1. Spectral editing

Under the same conditions (14 kHz MAS and full relaxation during the recycle delay), selective DP spectra of C not bonded to H and mobile segments were recorded after recoupled dipolar dephasing, with decoupling gated off during a 68 μs period centered on the 180° pulse of the Hahn echo before detection [37]. These spectra are shown scaled by a factor of 1.11 to correct for slight long-range C-H dephasing of the nonprotonated C signals, as is typical practice [37]. In other words, the spectrum after dipolar dephasing is slightly scaled up to match the peaks of the nonprotonated C=O peaks in the full DP spectrum. A CH-only spectrum was obtained by dipolar distortionless enhancement by polarization transfer (dipolar DEPT) [27] and a CH_2-only spectrum by three-spin coherence selection [29], both at 5.787 kHz MAS. For fully ^{13}C enriched samples, the experiment time was on the order of 2 h, while for partially ^{13}C enriched samples, the time was up to 17 h for CH and 25 h for CH_2 selection. The longest time was needed for the Glc-1h-180-LA sample, since only a relatively small amount of this material was available.

A 5-pulse chemical-shift anisotropy (CSA) dephasing pulse sequence followed by TOSS was applied at 5 kHz MAS [28]. The ^{13}C CSA filter was combined with an incrementation of the preceding z-period in four steps of $t_r/4$, which provides "γ-averaging" to ensure that TOSS suppresses the spinning sidebands up to fourth order. For dipolar dephasing, a period of 40 μs without ^{1}H decoupling was optionally added. The cross polarization (CP) contact time was 0.5 ms. With a recycle delay of 2 s, 448 transients were collected over 15 min for the ^{13}CGlc-1h-180-HA sample.

The hydroxyl-proton selection (HOPS) NMR experiment was applied to selectively polarize the OH-bonded nonprotonated carbons at 14 kHz MAS in ^{13}C-enriched solids [30]. In short, after a recoupled ^{1}H{^{13}C} dephasing period of 70 μs that also serves as a chemical shift filter (on resonance at 10.5 ppm) suppressing CH_3 proton magnetization, the retained OH proton magnetization is transferred to ^{13}C by 0.25 ms of cross polarization. HOPS spectra were obtained with measuring times of ≤2 h.

2.3.2. Two-dimensional NMR

A two-dimensional (2D) ^{1}H-^{13}C heteronuclear correlation (HetCor) spectrum [38] was recorded at 7.5 kHz MAS with frequency-switched Lee-Goldburg homonuclear decoupling [39] and total suppression of spinning sidebands (TOSS) before detection, with a cross-polarization time of 0.08 ms and a minimal mixing time of 0.01 ms, with the goal of detecting the characteristic peak of aldehydes (O=C-H) near (10 ppm, 179 ppm). In order to completely suppress strong overlapping peaks of nonprotonated carbons, the spectrum was CH_n-only edited, i.e., obtained as the difference between a HetCor spectrum acquired with short CP of 0.08 ms and its counterpart after dipolar dephasing.

Two-dimensional (2D) double-quantum/single-quantum (DQ/SQ) NMR spectra were measured at 14 kHz MAS with 0.57 ms of ^{13}C–^{13}C dipolar recoupling by SPC5 [40] without ^{1}H irradiation, relying on the ^{13}C irradiation at $|\gamma B_1|/2\pi = 70$ kHz for heteronuclear decoupling [31]. Recoupled dipolar dephasing of 68 μs duration [28] was applied before detection. The signal averaging time for each sample was up to 25 h.

Hydroxyl-proton selection [30] was combined with a two-dimensional dipolar-dephased DQ/SQ experiment to study the bonding environment of the nonprotonated C-OH groups, in particular in phenols. The pulse sequence for this not previously published experiment is shown in Fig. S1. The signal averaging time for each sample was up to 32 h.

Selective correlation of signals of nonprotonated or mobile carbons with those of neighboring protonated carbons was achieved in a simplified version of EXPANSE NMR [31] with 0.072-ms CP followed by 1 ms and 10 ms of ^{13}C spin diffusion and by recoupled dipolar dephasing before detection. The signal averaging time used for each sample was up to 38 h. An optional five-pulse ^{13}C CSA filter was applied (directly after CP in the EXPANSE pulse sequence, at 14 kHz MAS) to suppress the signal of aromatic CH, while retaining the signal of the sp^3-hybridized carbons. The signal averaging time used for ^{13}CGlc-1h-180-HA was 11 h.

A two-dimensional ^{13}C–^{13}C exchange NMR spectrum [41] was measured at 7 kHz MAS with high-power dipolar decoupling and TOSS before detection. A TOSS and an inverted TOSS four-pulse sequence were applied before and after the evolution time, respectively, to suppress the spinning sidebands in the ω_1 domain [39,42,43]. ^{1}H irradiation at a field strength that matches the MAS frequency (DARR) was applied during the mixing time to facilitate ^{13}C spin diffusion [44]. The mixing time was set to 1 s to allow for dipolar magnetization transfer over several bonds and thus probe the local environment of each carbon. For each ^{13}C-enriched sample, the signal averaging time was ~19 h.

2.3.3. Spectral simulations for hydrochar models

Empirical (database) chemical shift prediction using the ACD/Labs NMR Predictor program [45] was used extensively, see the SI, to assign specific cross peaks in the spectrally-edited ^{13}C–^{13}C 2D spectra. The predicted chemical shift was based on the hierarchically ordered spherical environment (HOSE) convention and thus atoms separated by more than three layers, unless connected by conjugated double bonds, were mostly ignored by the program.

Detailed structural models were generated for both of the fully-^{13}C-enriched hydrochar materials based on quantitative 1D and, indirectly, spectrally edited 2D ^{13}C NMR spectra as well as the elemental composition obtained from combustion analysis (C, H, and then O by difference), which provide relative amounts of key structural fragments and constrain the possible structural components. The highly crosslinked nature of the material is taken into account by excluding the structural units on the edge of the proposed network structural model. The models were refined by calculating 1D ^{13}C NMR spectra, both for all C and for nonprotonated or mobile CH_3 from dipolar recoupling, using the predicted chemical shift and the number of attached H provided by the ACD/Labs NMR Predictor program [45]. These data were then input into a MATLAB program for conversion into spectra with Gaussian line broadening of ca. 20 ppm full width at half maximum applied to all peaks from the proposed model except for the ^{13}CGlc-1h-180-HA model, where the levulinic acid peaks were broadened using a much smaller line broadening of ca. 5 ppm (due to the structural homogeneity of the small molecule). First-order aromatic spinning sidebands at 14 kHz MAS were also taken into account (2 × 5 % of the centerband intensity) considering the typical chemical shift anisotropy of carbons in oxygen-containing aromatic rings. The structural model was optimized iteratively by gradual modifications of the structure until the simulated and experimental spectra were in good agreement. As with previous examples in the hydrochar literature [10,16,25], each model should be thought of as a typical structural unit containing all of the key chemical features of the material.

3. Results

The objective of this work is to use advanced solid-state ^{13}C NMR methods to elucidate hydrochar structure in greater detail and with greater certainty than demonstrated in previous studies [4,11,26]. To that end, a series of hydrochar samples were synthesized from ^{13}C glucose at different reaction times and temperatures, in the presence and absence of differing amounts of homogeneous acid catalyst. The range of conditions was selected to be inclusive of the majority of studies published on hydrochar [6,46]. Hydrochar synthesis conditions used in the literature are listed in Table S3. Of the nine hydrochar samples, two end points in synthesis parameter space, ^{13}CGlc-1h-180-HA and ^{13}CGlc-5h-280-NA, were selected for detailed study, as these two samples bracketed most of the composition space of all others. Accordingly, the following discussion emphasizes these two samples.

3.1. Quantitative ^{13}C NMR spectra

Fig. 1 displays quantitative ^{13}C NMR spectra of four of the nine partially or fully ^{13}C-enriched hydrochars studied here, and the corresponding quantitative ^{13}C spectra of the nonprotonated carbons and mobile segments; spectra of all samples are shown in Fig. S2. The spectra are fairly similar and dominated by aromatic bands spanning a range from 105 to 155 ppm. Relatively sharp peaks at 210, 177, 37, and 30 ppm are at least partly attributable to the C=O, COO, CH_2, and $CH_2 + CH_3$ signals, respectively, of levulinic acid, as demonstrated by Baccile et al. [26]. The assignment to levulinic acid was confirmed by obtaining the difference spectrum of the original ^{13}CGlc-1h-180-HA material and the tetrahydrofuran (THF)-sonicated solid residue of ^{13}CGlc-1h-180-HA, see Fig. S3, showing the signals of levulinic acid, which is soluble in THF. Fractional areas of C=O, COO, aromatic, and other signals are listed in Table 1 for the nine samples studied here. They quantify the increase in the aromatic-carbon fraction observed in the spectra of Fig. 1.

The spectrum in Fig. 1a shows essentially the same peaks as the hydrochar sample studied by Baccile et al. [26], with similar intensity ratios. This demonstrates that hydrochar synthesis is reproducible in different laboratories and that our low-temperature (180 °C) samples are similar to that previously analyzed in Ref. [26]. Nevertheless, peak overlap makes assignments ambiguous, and our structural conclusions from advanced NMR with spectral editing, documented in the following, differ in important details, such as the abundance of phenols, from those in Ref. [26].

3.2. Spectral editing for peak assignment

Different types of functional groups may have overlapping ranges of ^{13}C NMR frequencies. Examples include ketones vs. aldehydes between 185 and 200 ppm, O-CHR-O vs. furan Cβ between 100 and 120 ppm, and phenol/alcohol C-OH vs. ether C-O-C from 140 to 160 ppm and 70–110 ppm. With spectral editing, these overlapping signals can often

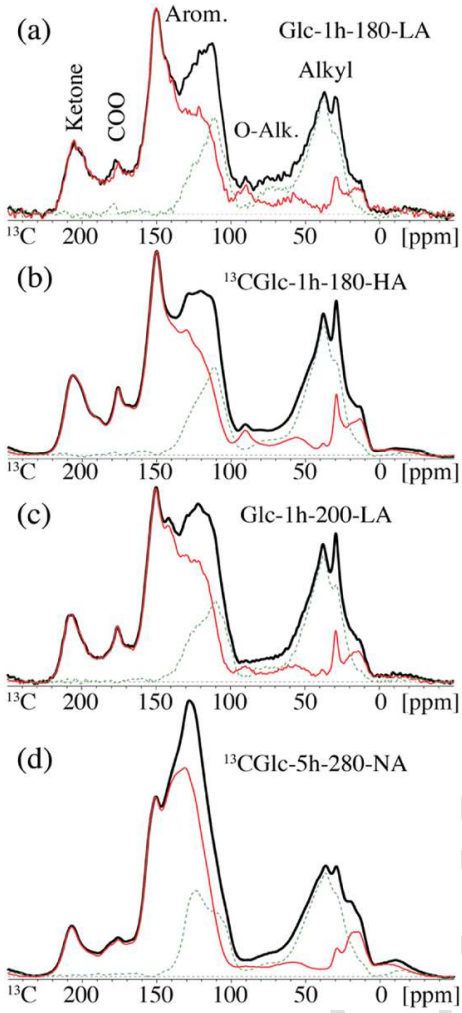

Fig. 1. Quantitative direct-polarization solid-state ^{13}C NMR spectra of (a) Glc-1h-180-LA, (b) ^{13}CGlc-1h-180-HA, (c) Glc-1h-200-LA, and (d) ^{13}CGlc-5h-280-NA. Bold black line: spectrum of all carbons; thin red line: spectrum of non-protonated carbons and mobile segments obtained after recoupled dipolar dephasing scaled by 1.11 to match nonprotonated carbon peaks; dashed green line: spectrum of protonated carbons obtained as the difference between the black and red spectra. The spectrum in (a) has a lower signal-to-noise ratio than the other spectra shown here due to limited sample amount and only partial ^{13}C enrichment.

be resolved, and peaks can be assigned reliably to specific functional groups. Comprehensive editing of one-dimensional spectra was applied to the glucose hydrochar samples studied here. Typical results for a low-temperature hydrochar, ^{13}CGlc-1h-180-HA, are shown in Fig. 2a and b. In the ^{13}C spectrum obtained after dipolar dephasing (purple spectrum in Fig. 2a), the CH and CH_2 signals are fully suppressed, while the signals of fast-rotating CH_3 groups resonating between 5 and 30 ppm are retained at a level of ~60 %. The nonprotonated sp^3-hybridized carbons (quaternary carbons, C_q) exhibit a broad band over the region of 50–70 ppm (from true quaternary carbons, $\mathbf{C}C_4$ or "C_q") as well as a distinctive peak at 90 ppm (from $O\mathbf{C}C_3$, or "OC_q"). Above 100 ppm, signals of nonprotonated C in the ranges of 110–160, 160–185, and 185–230 ppm can be assigned to aromatic, COO, and ketone/aldehyde carbons, respectively. CH_2 spectral editing by three-spin coherence selection [29], see the red trace in Fig. 2a, shows an intense band between 20 and 50 ppm, the signal of CH_2 groups bonded to two carbons (C-CH_2-C). In the range of OCH_2 resonances (60–75 ppm), only a weak broad peak is visible.

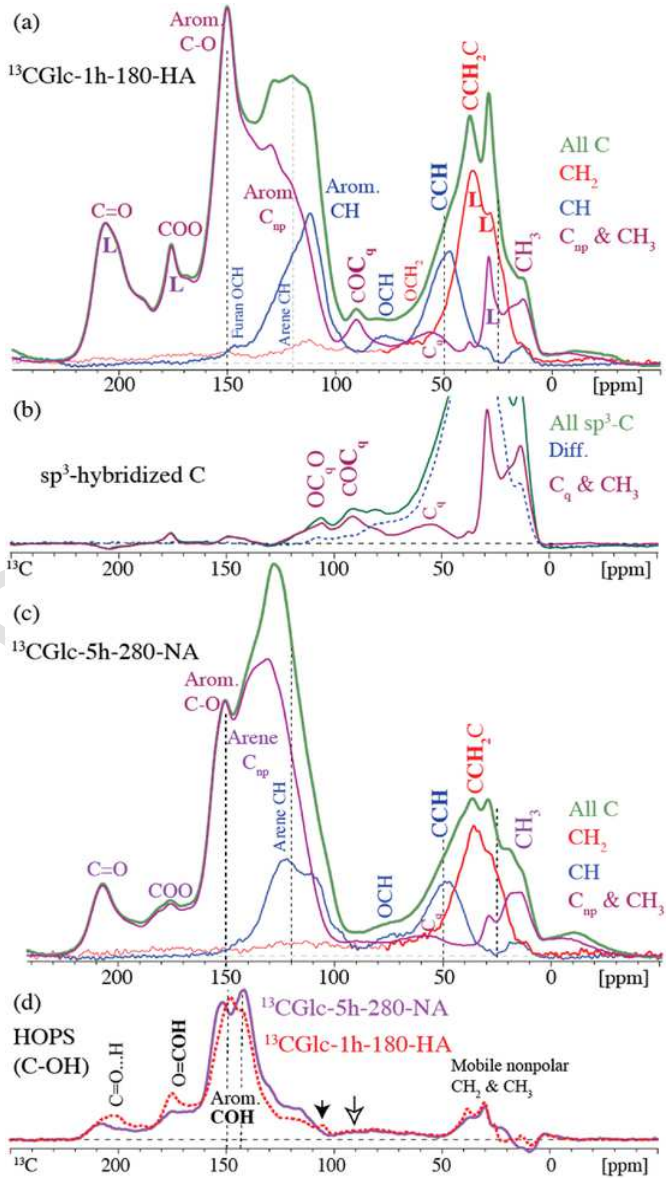

Fig. 2. Spectral editing of ^{13}C NMR spectra of (a, b) ^{13}CGlc-1h-180-HA and (c) ^{13}CGlc-5h-280-NA. (a) and (c) show quantitative spectra of all carbons (green lines); spectra of nonprotonated carbons and mobile segments obtained after recoupled dipolar dephasing (thin purple lines); spectra of CH carbons (thin blue lines); and spectra of CH_2 carbons (red lines). Peaks of levulinic acid are marked by "L" in (a). (b) shows the CSA-filtered spectrum of all sp^3-hybridized carbons (green line); the spectrum of nonprotonated sp^3-hybridized carbons and mobile segments obtained after CSA filtering and recoupled dipolar dephasing (purple line); and the difference spectrum of protonated carbons (dashed blue line). (d) Hydroxyl-proton selected (HOPS) spectra of both materials, showing mostly signals of C-OH groups. The presence of the O-C-OH signal at 104 ppm and the absence of the OC_q peak at 90 ppm is marked by arrows.

In the CH-only spectrum obtained after dipolar DEPT (blue trace in Fig. 2a), the sp^3-hybridized C-CH carbons exhibit a major peak at 35–60 ppm and O-CH carbons a clear foot at 65–85 ppm [27]. Beyond 100 ppm, the CH carbons are mostly aromatic CH (sp^2-hybridized) but can also derive from sp^3-hybridized O-CH-O. The latter can be observed selectively in a spectrum after a chemical-shift-anisotropy (CSA) filter, since sp^2-hybridized carbons have larger CSAs than sp^3-hybridized carbons and therefore can be efficiently suppressed while signals for sp^3-hybridized carbons are retained [28]. Fig. 2b shows a CSA-filtered CP

spectrum with and without C-H dipolar dephasing, where the suppression of the 100–150 ppm signals reveals the sp^2-hybridization of these carbons. In the spectrum after CSA filtering and dipolar dephasing (the purple trace in Fig. 2b), distinct peaks at 90 ppm and 104 ppm are observed, from oxygen-bonded nonprotonated carbons that are sp^3-hybridized.

Spectral editing applied to a representative high-temperature hydrochar, ^{13}CGlc-5h-280-NA, is shown in Fig. 2c. It reveals mostly similar peak positions as seen in Fig. 2a but with significant changes in relative intensities. Most prominently, more arene carbons are observed around 120–140 ppm, including arene CH near 122 ppm. The four sharp peaks of levulinic acid, which are prominent in Fig. 2a, are much less pronounced in Fig. 2c after high temperature synthesis. Furthermore, the 90-ppm signal of the nonprotonated sp^3-carbon (OC_q) is missing, showing that the oxygen-bonded quaternary carbons either do not form or are degraded when hydrothermal carbonization takes place at higher temperature.

The spectra in Fig. 1 contain a wide range of aromatic-carbon signals consistent with phenolic subunits, but the phenol content cannot be quantified from Fig. 1 due to substantial overlap with furan signals. Hydroxyl-proton selective (HOPS) ^{13}C NMR experiments were performed to overcome this limitation and the resulting spectra of both ^{13}C-enriched samples are shown in Fig. 2d. The HOPS spectra are dominated by two phenol peaks, one near 142 ppm from *ortho*-diphenols, the other near 149 ppm for 180 °C and near 152 ppm for 280 °C synthesis temperature from monophenols or *para*-diphenols. The absence of a peak at 90 ppm proves that the OC_q carbon is not bonded to an OH group but to an oxygen atom that participates in an ether or ester bond. The presence of catecholic *ortho*-diphenols in both materials, further confirmed by 2D NMR below, is especially important given the role of oxygen-containing functional groups in heavy metal cation adsorption [47,48].

3.3. Effect of synthesis time

Fig. S4 compares pairs of ^{13}C NMR spectra of three hydrochars synthesized at the same temperature and acid content for 1 h and 5 h. The line shapes of each pair are similar. The biggest change observed is a moderate increase in aromaticity from 1 h to 5 h at 280 °C. These results indicate that few structural transformations take place after 1 h [7], meaning that a multi-step formation mechanism consisting of different types of pathways at early formation times and late formation times is not required. Future work might evaluate earlier synthesis times to determine if initial nucleation involves the same pathways as subsequent hydrochar growth; this work was limited to evaluating materials at longer times when sufficient quantities (tens of milligrams) of hydrochar have formed.

3.4. 2D EXPANSE NMR

A hydrochar model consisting of furan and arene (phenol) sub-units connected through cross-linking groups emerges from the spectra in Figs. 1–3. How these structural subunits are linked to one another can be determined by two-dimensional ^{13}C–^{13}C NMR with spectral editing. Fig. 3 shows 2D EXPANSE ^{13}C spectra of the ^{13}CGlc-1h-180-HA and ^{13}CGlc-5h-280-NA samples. The spectra exhibit cross peaks due to local ^{13}C–^{13}C spin exchange from CH_n to nonprotonated C [31]. The complementary spectral editing suppresses the trivial diagonal ridge with its associated artifacts and resolves peak overlap, in particular between 50 and 100 ppm in the detection (horizontal) dimension. All strong and some of the weak peaks present in Fig. 3 are attributable to one-bond transfers. Weak peaks from two-bond transfer may be observed for the most abundant structural moieties. The complementary selection of CH_n signals in the evolution and nonprotonated-C peaks in the detection period removes most of the otherwise dominant signal along the spectral diagonal [31]. This provides excellent dynamic range and enables detection of small cross peaks. Most importantly, cross peaks near the diagonal can be detected, which in particular enables identification of arenes, which have resonances that cluster between 120 and 140 ppm. Since the magnetization starts from a CH_n of known frequency in the vertical and ends on a nonprotonated C of known frequency in the horizontal dimension, most cross peaks contain specific structural information.

In the ^{13}CGlc-1h-180-HA sample, see Fig. 3a, the magnetization of CH_3 at 12 ppm transfers to furan-Cα resonating at 158 ppm, and that of CH_3 at 26 ppm to ketone-C in a 2-acetylfuran structural unit. The underlying structures are shown in the Figure. The weak CH_3 signal at (105 ppm, 12 ppm) indicates some two-bond correlation between sp^2-CH and CH_3; as expected, it is not seen in the corresponding spectrum with a short mixing time of 1 ms, see Fig. S5a, where only one-bond correlations are observed prominently.

Sharp cross peaks of levulinic acid are observed at (30 ppm, 177 ppm) and (30 ppm, 208 ppm). More generally, the magnetization of CH_2 carbons resonating at ~40 ppm transfers to neighboring quaternary carbons (broad 50–80 ppm C_q, sharp 90 ppm OC_q), furan-Cβ (129 ppm), -Cα (149 ppm), and furan-bonded ketone (189 ppm). A particularly distinctive cross peak is observed between CH_2 at 26 ppm and furan-Cα at an elevated chemical shift (154 ppm). According to Fig. S6, these chemical shifts are characteristic of one or two bridging CH_2 between a furan α carbon and another furan ring or a phenol β-carbon, with limited methylene chemical shift variations (due to the absence of other substituents). The furan chemical shift >152 ppm indicates a linkage of the other furan α-carbon on the same ring to sp^2-hybridized C, e.g., of ketones, see Fig. S7. In the frequency range of 45–55 ppm in the vertical dimension, which is characteristic of sp^3-hybridized CH according to Fig. 2a and c, featureless intensity is observed but no resolved cross peaks can be discerned.

The magnetization of sp^2-hybridized CH resonating at >100 ppm in the vertical dimension transfers to nonprotonated (substituted) furan-Cβ (125 ppm), substituted furan-Cα (~152 ppm) or monophenols, and substituted arenes including *ortho*-diphenols (125–145 ppm). In a CSA-filtered 2D EXPANSE spectrum, see Fig. S5b, all the cross peaks at > 100 ppm in the vertical dimension are suppressed, proving that these CH carbons are sp^2-hybridized. This is consistent with the small sp^3-CH signal intensity at >100 ppm in the one-dimensional CSA-filtered ^{13}C spectra of Fig. 2b.

The lower left corner of the spectrum in Fig. 3a shows weak peaks that must be attributed to = CH–C = O fragments of alkenes, or to unexpected two-bond correlations of substituted aromatic rings; the assignment to alkenes bonded to ketones is supported by the presence of these signals in the 1-ms (one-bond) spectrum of Fig. S5a and their absence from the spectrum of the high-temperature hydrochar (where an alkene-quinone = CH–C = O cross peak is observed instead). Other evidence of alkenes will be presented below. Alkenes have not previously been detected conclusively in hydrochar, and their presence suggests potential anchoring points for post-synthesis functionalization.

3.5. 2D solid-state INADEQUATE NMR

A complementary two-dimensional ^{13}C–^{13}C NMR spectrum with spectral editing and free of a trivial diagonal ridge can be obtained using dipolar-dephased double quantum/single quantum (DQ/SQ) NMR [31]. It is analogous to the INADEQUATE experiment in solution NMR, but due to dipolar dephasing selectively shows cross peaks only between directly bonded carbons not bonded to H or between nonprotonated C and a CH_3 group. Fig. 4 and Fig. S8 present 2D dipolar-dephased DQ/SQ ^{13}C spectra of ^{13}CGlc-1h-180-HA and ^{13}CGlc-5h-280-NA, respectively, excited by 0.57-ms recoupled excitation and reconversion times. As in the conceptually related INADEQUATE experiment, a directly bonded nonprotonated ^{13}C–^{13}C spin pair (or $^{13}C_{np}$ and a $^{13}CH_3$

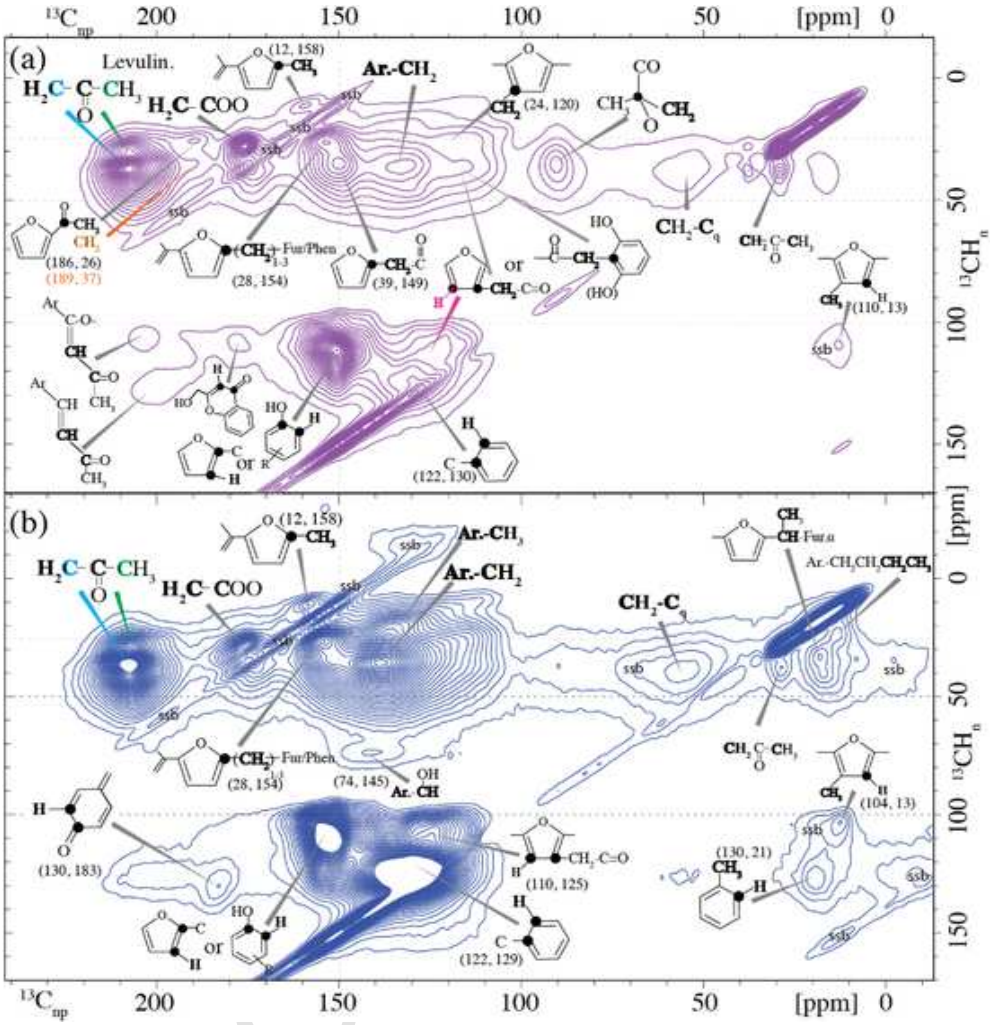

Fig. 3. Spectrally edited two-dimensional ^{13}C exchange NMR of (a) ^{13}CGlc-1h-180-HA and (b) ^{13}CGlc-5h-280-NA, showing cross peaks between CH_n (vertical dimension) and nearby nonprotonated carbons or carbons in mobile segments (horizontal dimension). The most relevant peaks are assigned to bonds between the highlighted atoms in the structures shown. Here, "Ar" and "Fur" refer to arene ring and furan ring, respectively. The spinning frequency was 14 kHz, the mixing time 10 ms. Spinning sidebands are marked "ssb".

group) gives rise to a pair of signals in the horizontal dimension at their sum chemical shift in the vertical dimension. Various resolved peak pairs are connected by colored horizontal lines added to the spectra. A line of a certain color indicates connectivity in a specific structural fragment.

In the DQ/SQ spectrum of ^{13}CGlc-1h-180-HA, one can observe signal pairs of CH_3 bonded to arene (black dashed), furan Cα (solid orange), furan Cβ (dashed orange), alkene C (brown), and C=O in levulinic acid (purple). Blue lines highlight that the nonprotonated carbon indicated by the peak at 50 ppm connects to arene carbons (broad peak centered at 133 ppm) and to a ketone carbon at 205 ppm. The dark green line traces out a 2-acetylfuran fragment, where a ketone at 189 ppm is connected to a CH_3 at 26 ppm and to a well-resolved furanic C-O at ~151 ppm. The chemical shift <153 ppm rules out substitution of the other α-carbon by C=O (see Fig. S9). The brown line for the well-resolved O-C_q resonating at 91 ppm, with bonds to three other carbons, highlights that it is bonded to CH_3 resonating at 22 ppm, and a ketone at 203 ppm, whose chemical shift indicates [31] that it is connected to an arene carbon (possibly at 135 ppm). In addition, the EXPANSE spectrum shows that the third C-C bond of the 90-ppm OC_q links it to CH_2. Similarly, the light blue line connects the O-C_q-O at 104 ppm, which has two C-C bonds, with CH_3 at 21 ppm and a ketone at ~195 ppm. The aromatic carbons show furanic and phenolic Cα and substituted-Cβ signal pairs, which were also observed in a DQ/SQ spectrum of "^{13}CGlc-60h-180-NA" reported by Baccile et al. [26].

The signals of many other types of other nonprotonated aromatic carbons are severely overlapped, making it difficult to resolve specific directly bonded spin pairs. Nevertheless, one can make conclusions about certain groups of spin pairs. Aromatic C-O and the Cβ carbons to which they are bonded account for the most intense signal ridges. Cβ-Cβ pairs of furans and/or phenols in different rings, or both substituted in the same furan ring, account for intensity near (2 × 115 ppm, 115 ppm). An intense and fairly distinctive peak at (280 ppm, 129 ppm) is consistent with arene–Cα-furan bonds. The central peak near (2 × 137 ppm, 137 ppm) can be safely assigned to arenes, because in furans pairs of nonprotonated carbons with chemical shifts between 132 and 145 ppm are extremely rare. The characteristic signal of pairs of directly bonded ketones [49] is not observed; while their resonance position around (2 × 200 ppm, 200 ppm) is outside the spectral region shown in Fig. 4, spectral plots that include it (see Fig. S10) do not show such resonances on the slope-two diagonal.

In the DQ/SQ spectrum of ^{13}CGlc-5h-280-NA, see Fig. S8, a pronounced increase in the arene carbon signal on the slope-two diagonal (i.e., near (2 × 137 ppm, 137 ppm)) can be observed, as expected from

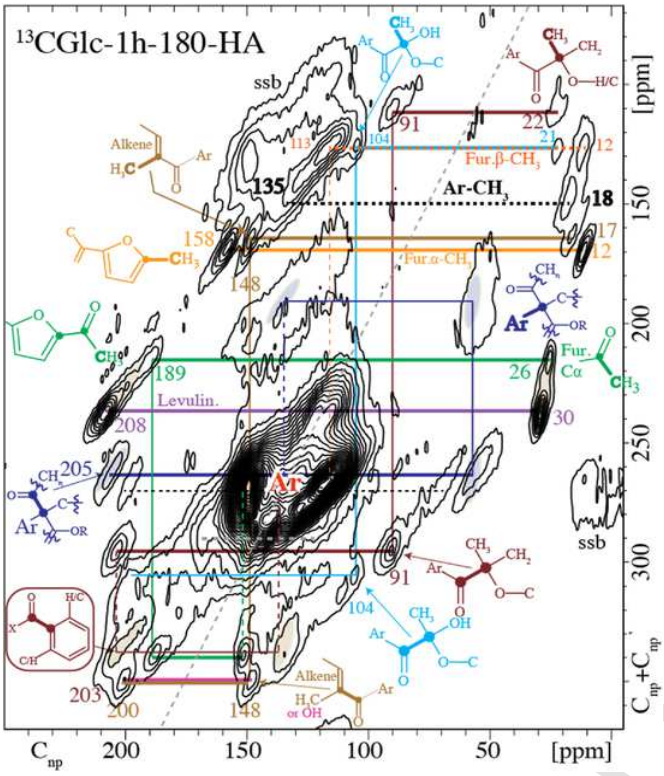

Fig. 4. Dipolar dephased DQ/SQ (double quantum/single quantum, solid-state INADEQUATE) ^{13}C–^{13}C NMR spectrum of ^{13}CGlc-1h-180-HA showing cross peaks between directly bonded nonprotonated carbons or of nonprotonated C with a CH_3 group. Color-coded structural assignment of most of the resolved peaks are shown. Spinning sidebands are labeled "ssb". The corresponding spectrum of ^{13}CGlc-5h-280-NA is shown in Fig. S8.

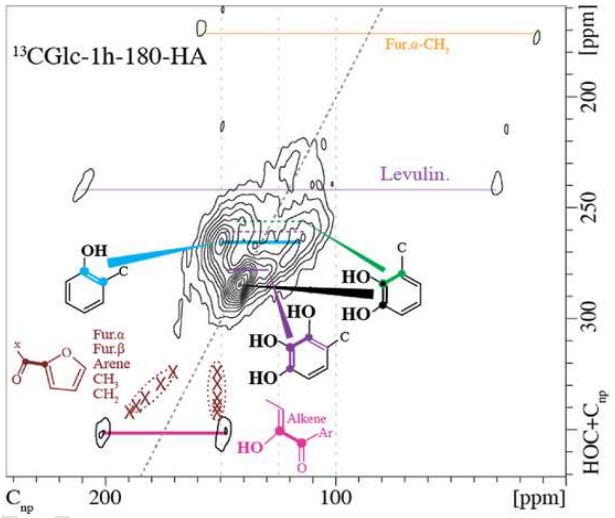

Fig. 5. Hydroxyl-proton selective (HOPS) DQ/SQ ^{13}C NMR spectrum with dipolar dephasing of ^{13}CGlc-1h-180-HA. The HOPS filter was applied before 0.25-ms CP to select C-OH signals; due to the generation of double-quantum coherence, peaks of nonprotonated carbons bonded to C-OH are also observed. The corresponding, fairly similar-looking spectrum of ^{13}CGlc-5h-280-NA is shown in Fig. S13.

the corresponding peak in the 1D spectrum of Fig. 1d. Another emerging structural feature (marked by the light-green line in Fig. S8) corresponds to a ketone at ~180 ppm that connects furan-Cα with an arene ring, in agreement with chemical-shift trends for ketones [31]. On the other hand, several of the spectral features observed in Fig. 4 are strongly reduced here, including peaks of C_q-containing structures (brown, light-blue), 2-acetylfuran (green), the arene-ketone-enol structure (pink line) and levulinic acid, indicating that these structural fragments are less likely to form or persist at higher than at lower temperature and without than with acid.

3.6. 2D NMR of phenols

Distinguishing furans and phenols is a key challenge in NMR analysis of hydrochar and similar oxygen- and aromatic-rich organic materials. Furans and phenols both contain aromatic C-O moieties that resonate between 147 and 163 ppm and consequently overlap in their 1D and 2D spectra. The important phenol signals can be characterized selectively by HydrOxyl Proton Selection (HOPS) with short cross polarization followed by a two-dimensional DQ/SQ experiment with dipolar dephasing (see Fig. S1 for the pulse sequence). The resulting spectrum shows signals of C-OH groups and of nonprotonated carbons to which they are bonded. Fig. 5 presents the HOPS-DQ/SQ spectrum of ^{13}CGlc-1h-180-HA. There is a pronounced on-diagonal peak at (2 × 142 ppm, 142 ppm). It arises from a pair of similar nonprotonated = C-OH carbons resonating at 142 ppm and must therefore be assigned to a structural unit of (HO-C_{np}) = (C_{np}-OH), which we refer to as an *ortho*-diphenol. The corresponding peak in the unselective DQ/SQ spectrum had previously been assigned to a linkage from furanic-Cα to furanic-Cα [26], which can be excluded now since that structure does not involve hydroxyl groups but only ethers. In the same spectrum, a phenol C-OH carbon at ~156 ppm connects with a nonprotonated aromatic carbon (~120 ppm), marked in light blue. Signals compatible with a 1, 2, 3-triphenol (see Fig. S11d) are also labeled in the figure.

In addition, near its lower edge, the spectrum exhibits a clear pair of peaks corresponding to a 200-ppm carbon (ketone) bonded to a nonprotonated aromatic or alkene C-O resonating at 148 ppm (pink line). Since these peaks are observed in the HOPS-DQ/SQ spectrum, there must be an OH group bonded to the nonprotonated-C at 148 ppm. The structure is recognized as an enol that is stabilized by the ketone neighbor [49]. Judging by the ketone chemical shift [31], the ketone may also be bonded to an arene ring. This can further delocalize the π electrons and stabilize the enol structures. Predicted chemical shifts for this enol structure shown in Fig. S12 confirm this assignment.

Enols are not generally considered thermally stable functional groups and would likely not survive hydrothermal conditions, meaning that this unexpected assignment requires additional confirmation. Attempts to explain these cross peaks by non-alkene structures were unsuccessful. The 148-ppm peak cannot arise from a phenol because phenol C-O is always bonded to aromatic C, not ketones. Even if the requirement of bonding to OH is relaxed, the signal would be difficult to explain otherwise: If it were from furan-Cα bonded to a ketone, the ketone-C would resonate at < 190 ppm [31], regardless of the other bonding partner of the ketone (including furan-Cα, -Cβ, arene, CH_3, and CH_2, which are indicated by brown "X" marks in Fig. 5), not at 200 ppm as observed experimentally. Thus, the conjugated enol structure is doubly justified, first by the chemical shift and then by the C-OH structure documented by HOPS selection.

3.7. Aldehyde signal

Aldehydes are thermally reactive H-C = O groups [50] which readily undergo acid or base-catalyzed aldol condensation [51] and whose signals overlap with those of ketones and carboxylic acids but can be distinguished by spectral editing due to the attached proton in the H-C = O group. Samples produced at low proton concentration and moderate temperature showed a characteristic 179-ppm signal of an aldehyde af-

ter spectral editing, see Fig. 6 and Fig. S2. As with enols, aldehydes are not considered to be thermally stable because they are prone to undergo aldol condensations with one another, producing ketones. In fact, aldol condensation is one of the main reactions implicated in hydrochar formation [11,47,52]. It may come as some surprise then that aldehydes are detected. Hydroxymethylfurfural (HMF) is a known aldehyde intermediate in thermal conversions of glucose [53], and has been observed by HPLC in hydrochar made at low temperature, see Table S2. That stated, the conventional thinking is that HMF is incorporated into hydrochar by means of aldol condensation, thereby converting the aldehyde group into a ketone [20,26]. The required strong evidence for the aldehyde assignment can be provided by spectral editing and 2D NMR, see Fig. 6. Aldehydes are nearly unique as protonated carbons resonating at >175 ppm. The CH_n-only spectrum of Glc-1h-200-NA (green trace in Fig. 6a) shows a small but distinct CH peak at 179 ppm. The characteristically high chemical shift of the attached proton (~10 ppm) observed in the ^{1}H-^{13}C HetCor spectrum of Fig. 6b confirms the assignment to an aldehyde. An EXPANSE ^{13}C–^{13}C cross peak at (179, 152) ppm (inset in Fig. 6a) shows that the aldehyde is bonded to a furan ring (H-C=O cannot substitute aromatic C-OH, which is only bonded to aromatic carbons). This documents five of the six carbons of HMF; the chemical shift of 152 ppm further suggests (see Fig. S7) that the sixth carbon, the substituent of the other furan Cα, is sp^3-hybridized, as in HMF. The dipolar dephasing and cross peak widths indicate that the HMF-like fragment is immobilized in the solid matrix. Integration of the aldehyde peak and accounting for the other five carbons in HMF gives HMF concentrations as follows: Glc-1h-180-LA: 2.3%C; Glc-1h-200-NA: 2.9%C; Glc-5h-200-NA: 1.3%C. In summary, HMF accounts for 1–3 % of all carbon in the low-temperature, low-acid materials, and for <1 % in the other six samples studied.

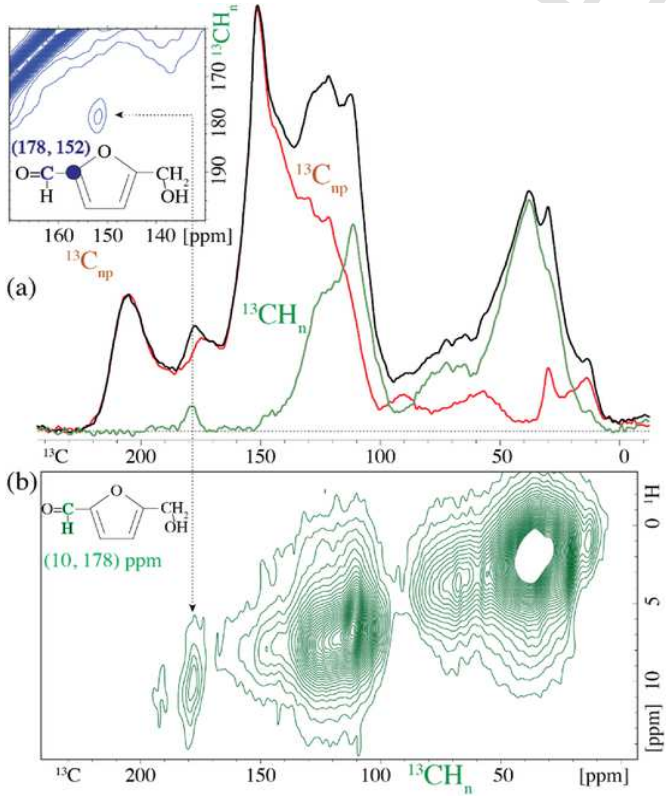

Fig. 6. (a) Full (black line), dipolar-dephased (red), and CH_n-only (by difference; green) ^{13}C NMR spectra of Glc-1h-200-NA. The inset shows the characteristic cross peak of the 179-ppm aldehyde O=CH in the EXPANSE spectrum. (b) CH_n-only edited ^{1}H-^{13}C HetCor spectrum obtained as the difference between a 0.08-ms CP HetCor spectrum and its counterpart after dipolar dephasing.

3.8. 2D exchange ^{13}C NMR with long mixing times

Some previous hydrochar models suggested a core–shell structure of the observed spherical particles, with a hydrophilic shell of ≥10 nm thickness surrounding a hydrophobic, aromatic-rich core [9,10]. Two-dimensional ^{13}C NMR with ^{13}C spin diffusion can be used to test if domains of different composition, e.g., alkyl-rich vs. aromatic-rich, are in close proximity to each other. We used 2D ^{13}C–^{13}C correlation experiments with a fairly long mixing time of 1 s at a moderate spinning frequency of 7 kHz, which allows ^{13}C magnetization to spread over a few nanometers [54]. A one-dimensional horizontal slice at a specific frequency, e.g., of a ketone, in the vertical dimension shows the spectrum of the functional groups reached by magnetization from the ketone. Materials that are compositionally inhomogeneous on the 5-nm scale will show various spectral patterns in their horizontal cross sections. Indistinguishable patterns for magnetization originating from all kinds of functional groups (ketones, COO, aromatic C-O, aromatic C-H, CH_2, and CH_3) as observed in Fig. 7 and Fig. S14 document compositional homogeneity on the 5-nm scale. Accordingly, the core–shell hydrochar model [9,10] can be rejected, at least for hydrochars made from soluble precursors.

4. Discussion

All the NMR spectra above, combined with elemental analysis by combustion, provide the data required to deduce representative or characteristic hydrochar substructures. In the following, evidence for various important structural units and their interlinkages is discussed, beginning with a review of the relative abundance of different functional groups present in hydrochar and culminating in proposed representative structural models containing these functional groups.

4.1. Abundant alkyl-bonded ketones

The ^{13}C NMR spectra of all hydrochar samples shown here exhibit significant ketone signals between 188 and 220 ppm. These were quantified by integration and normalization to the total ^{13}C NMR signal area as summarized in Table 1. In the samples investigated here, ~5–9% of carbons are from ketone groups, implying that 15–25 % of all carbons are ketones or bonded to ketones. The abundance of ketones explains the numerous ketone-related cross peaks in the 2D spectra of Figs. 3 and 4. Increasing reaction temperature decreased the ketone fraction (e.g., 180 °C: 8.9 ± 0.3 % → 200 °C: 7.8 ± 0.4 % → 280 °C: 5.8 ± 0.5 %).

4.2. Phenols vs. furans

Since hydrochar is both aromatic- and oxygen-rich, it contains abundant aromatic C-O units, whose resonance near 150 ppm is often the highest peak in the ^{13}C NMR spectrum, see Fig. 1. Both furans and phenols contain such aromatic carbons bonded to oxygen, resulting in overlapping signals and ambiguous peak assignment in unselective one-dimensional NMR spectra. In some studies, the aromatic C-O peaks were assigned to furans [26], in others to phenols or phenol ethers [9,10]. In our study, advanced NMR approaches with hydroxyl-proton selection (HOPS) have been applied to distinguish furans and phenols from one another. Importantly, signals exclusive either to furans (Figs. 3a and 4) or to phenols (Figs. 2d and 5) are observed in the spectra of a single hydrochar material, proving the coexistence of both types of aromatic rings. The presence of phenols also explains the OH signal detected in FT-IR and reported in previous studies [20,55].

Apart from the shared aromatic C-O signal, furans and phenols actually show rather different overall spectral patterns and the appearance

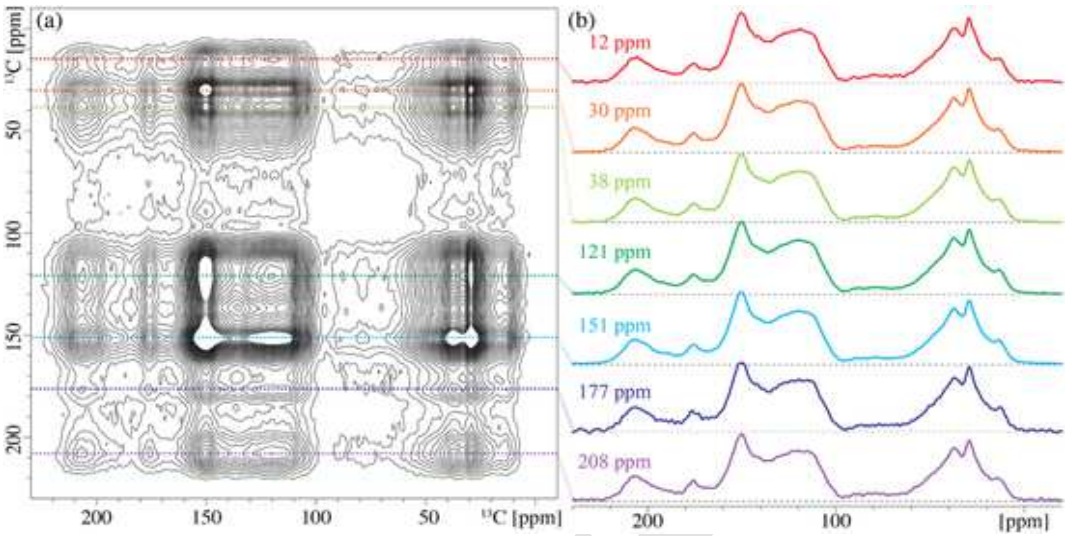

Fig. 7. (a) Two-dimensional ^{13}C spin exchange spectrum of ^{13}CGlc-1h-180-HA with a mixing time of 1 s. (b) Horizontal slices of the spectrum in (a) taken at the indicated positions in the vertical dimension, scaled to the same maximum peak intensity; the chemical shift values of the vertical slices are indicated by the same color code as the dashed lines in (a). From bottom to top, the (chemical shift, color, carbon) triples are: (208 ppm, purple, ketone C=O), (177 ppm, blue, COO), (151 ppm, cyan, aromatic C-O), (121 ppm, dark green, aromatic C-H), (38 ppm, light green, CH_2), (30 ppm, orange, levulinic acid CH_3), and (12 ppm, red, CH_3). The corresponding, similar-looking figure for ^{13}CGlc-1h-180-HA is shown in Fig. S14. Spinning frequency: 7 kHz. TOSS-based spinning sideband suppression was used in both dimensions.

of specific secondary peaks can partially differentiate one from the other. In quantitative 1D^{13}C NMR spectra, furan rings always produce two baseline-resolved peaks of equal intensity, one between 138 and 163 ppm, the other between 100 and 132 ppm. Accordingly, the ^{13}C NMR spectrum of a polymer consisting mostly of furan rings, polyfurfuryl alcohol [56], shows nearly baseline resolution between C-O and *C*H-C-O resonances centered near 155 and 110 ppm [57,58]. The furan sub-spectrum obtained from the model in Fig. 8 (blue dashed lines)

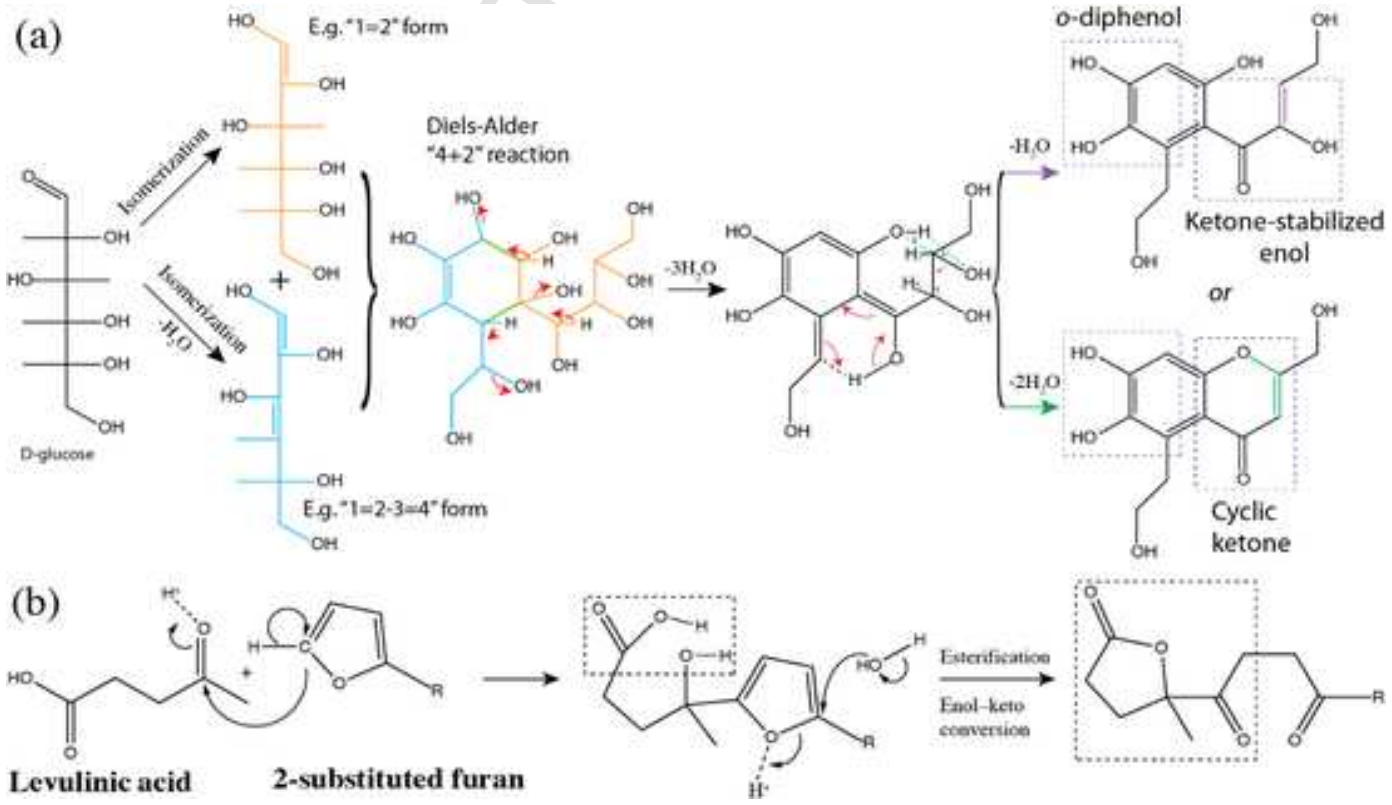

Fig. 8. Possible reaction routes: (a) from glucose to an *ortho*-diphenol and a ketone-bonded enol or cyclic ketone, and (b) from levulinic acid and a furan to CH_2-C_q (C=O)(O)-CH_3 with C_q resonating near 90 ppm.

clearly confirms this pattern of two equal-area and baseline-resolved peaks. This contrasts with the full spectrum of hydrochars, see Fig. 1, which additionally shows strong intensity around 130 ppm that indicates the presence of a significant arene component, an assignment that includes phenols.

The signals from phenols, whose C-O sites account for only one or two out of six aromatic carbons, are much more varied and spread out, see Fig. S11, than the two peaks of furans. In a monophenol or *para*-diphenol, the C-O peak between 145 and 165 ppm has only half of the intensity of the signal of the neighboring (i.e., *ortho*) carbons resonating between 100 and 135 ppm. In monophenols, three additional carbons resonating between 115 and 142 ppm fill in the center of the aromatic-signal range; *ortho*-diphenols contribute intensity near 143 ppm. The arene/phenol subspectrum obtained from the model in Fig. 8 (red dash-dotted line) confirms this.

4.3. Polyphenols

The HOPS-filtered DQ/SQ experiment introduced in this work provides compelling evidence for catecholic *ortho*-diphenols resonating near 142 ppm. These were previously misassigned to furan-furan α–α linkages [26] since both are symmetric, aromatic O-(C =)-(=C)-O structures. HOPS proves HO-C-C-OH structures, which are not present in furan rings. A mechanism for *ortho*-diphenol formation is proposed below. Fig. S15 documents that furan α–α linkages would vary significantly in resonance frequency (from about 133 to 157 ppm) depending on the substitution of the two rings by ketones or other furan rings, while the observed diagonal peak in the HOPS-filtered 2D spectrum of Fig. 5 is less broad than this range. It is interesting to note that diphenols have the same C:O ratio of 3:1 as the sample as a whole.

The HOPS spectra in Fig. 2d show the COH groups of *ortho*-diphenols in a 1:1 ratio with single phenols. The spectra indicate that both types of phenols are similarly generated at low and high temperatures. *Meta*-di- and tri-phenols do not appear to be common; they have characteristically extreme chemical shifts of 158 ppm and 103 ppm (see Fig. S11), neither of which are prominently observed in our spectra. *Para*-diphenols may be present since their chemical shifts resemble those of monodiphenols except for a 4-ppm lower C-OH chemical shift (see Fig. S11), which would actually explain the low-temperature hydrochar results better, while the 280 °C hydrochar shows the chemical shift predicted for real monodiphenols. Signals compatible with 1,2,3-triphenols are seen at moderate intensity levels in the HOPS-filtered 2D spectrum of the 180 °C hydrochar, see Fig. 5, but not at all in that of the 280 °C hydrochar, see Fig. S13.

4.4. Furans

Unambiguous identification of furan signals in the presence of phenols is achieved most convincingly in spectrally edited 2D ^{13}C–^{13}C NMR spectra. Here, furan rings show characteristic signals of aromatic C-O bonded to C=O (in DQ/SQ spectra with dipolar dephasing, bottom of Fig. 4), to CH_2 and CH groups (in EXPANSE spectra, near the top of Fig. 3a and b), and to CH_3 groups (in both types of 2D ^{13}C–^{13}C spectra). All of these are specific to furan C-O since phenol C-O is only bonded to aromatic C. Furans also produce characteristic strong reductions in the chemical shifts of ketones to which they are bonded [31], giving rise to a strong shoulder around 190 ppm, see Fig. 2. The furan-bonded aldehyde characteristic of HMF has been resolved by spectral editing, see Fig. 6 and Fig. S2, in hydrochars synthesized at low temperature and acid concentration.

Furan chemical shifts are useful indicators of the furan substitution pattern. The simulations in Fig. S6, Fig. S7, Fig. S9, and Fig. S15, summarized in Tables S4-S8, indicate that electron-withdrawing groups such as C=O and COO at furan-Cα' and/or Cβ increase the Cα chemical shift to >155 ppm, while electron-donating groups such as *o*-phenol or CH_2-R decrease it to <149 ppm.

4.5. Arenes

The presence of arene fragments is clearly established in the EXPANSE spectra. These exhibit signals of arene CH, resonating between 125 and 139 ppm, bonded to nonprotonated arene C that resonates between 123 and 140 ppm. In a simple 2D exchange spectrum without spectral editing, the cross peaks from these carbons are hidden by the large diagonal ridge and therefore cannot be convincingly identified.

Arenes are also proved by strong cross peaks near 140 ppm, the characteristic frequency of substituted arene C, with alkyl C (near 40 ppm) in the EXPANSE spectra of Fig. 3 and near 135 ppm with C=O groups (200 ppm) in the DQ/SQ spectrum of Fig. 4. These signals are distinct from those of correspondingly substituted furan carbons, which would resonate at <130 ppm (substituting furan-Cβ) or >147 ppm (bonded to furan-Cα). The strong cross peaks between arenes and alkyl substituents in Fig. 3 and with ketones in Fig. 4, as well as the full equilibration in the spectrum of Fig. 7, show that the arenes are incorporated into the rest of the structure and are not part of a distinct hydrochar core or shell. The arene fraction increases with increasing synthesis temperature, corresponding to an increase in overall aromatic content, see Table 1.

4.6. Alkenes

Alkenes (isolated C=C structures) are difficult to identify in unselective 1D spectra because they resonate in the same spectral range (110–160 ppm) as aromatic moieties. Furthermore, the abundances and signals of alkenes tend to be relatively low since an individual alkene contains only two carbons, while a furan ring contains four and an arene, including a phenol, at least six. In principle, alkenes can sometimes be identified in ^{1}H-^{13}C HetCor NMR via the lower chemical shift (5–7 ppm) of their protons compared to arene (6.5–8.5 ppm) and furan (6–7.5 ppm). However, in practice the alkene ^{1}H NMR signals are still difficult to detect since they tend to be overwhelmed by nearby aromatic signals, or the alkenes may be substituted.

Our spectral editing has revealed a few characteristic alkene signals. Examples include = CH resonating near 150 ppm in CH- or CH_n-only spectra, and = C-OH bonded to a ketone in HOPS-filtered DQ/SQ spectra, see Fig. 5. Two peaks near (105 ppm, 203 ppm) in the EXPANSE spectrum of Fig. 3a also suggest alkene structures (O-C=CH-C=O). All alkene signals are much reduced in the high-temperature hydrochar sample, consistent with the thermal reactivity of alkenes.

4.7. Alkyl linkers

Hydrochars, even those made at high temperature, always contain a significant fraction of sp^3-hybridized CH_2 and CH groups. The EXPANSE spectrum in Fig. 3 shows strong signals of CH_2 groups bonded to ketones, furans, and arenes. This indicates that aromatic rings and alkyl segments are connected on the scale of individual bonds. In Fig. 3, specific signals of CH_2 groups linking furan rings and C=O groups are detected.

4.8. Formation of distinctive structures in low-temperature ^{13}CGlc-hydrochar

Diverse structural features such as alkenes and nonprotonated carbons at 90 ppm are detected in the low-temperature high-acidity sample, ^{13}CGlc-1h-180-HA, more so than in the high-temperature hydrochar. These structures are not changed much when the acid concentration is altered (see Fig. S2). In the following, these moieties and potential pathways for their formation are discussed in more detail.

In the HOPS-filtered dipolar-dephased DQ/SQ spectrum of Fig. 5, a ketone-stabilized enol structure, arene-C(=O)-C(OH)=C, can be recognized. It has been proposed that a ketone-stabilized enol can form by aldol addition/condensation of HMF molecules [49]. Another possible reaction mechanism that accounts for the formation of this structure is depicted in Fig. 8a. It accompanies the formation of an *ortho*-diphenol via a [4 + 2] Diels-Alder reaction of, for example, a 1-mono-ene and a 1,3-di-ene easily obtained from the isomerization and dehydration of glucose.

Another distinctive feature of low-temperature hydrochar is 90-ppm ether O-C_q bonded to ketone, methylene, and methyl groups. Fig. 8b shows how it can form by nucleophilic addition of a furan-Cα to the ketone of levulinic acid. The chemical shift of the resulting quaternary carbon of the five-membered cyclic intramolecular ester has been confirmed by empirical chemical-shift simulation, which predicts a peak position of 90 ± 4 ppm. The lack of an OH group bonded to this carbon is in good agreement with the absence of this 90-ppm peak from the HOPS spectrum in Fig. 2d.

4.9. Effects of hydrothermal synthesis conditions on structure

It has been documented in the literature that hydrothermal carbonization can be affected by the precursor, time, acidity, and temperature of reaction [6–8]. In this work, the overall line shapes of quantitative ^{13}C spectra have been shown to be similar for samples produced under various conditions, see Fig. 1 and Fig. S2, indicating that a similar basic structure holds for all the hydrothermally carbonized samples. Increasing reaction time to over 1 h produces only very limited changes in composition (see Fig. S4). Acidity and synthesis temperature moderately alter structural details: increasing acid concentration decreases HMF and increases levulinic acid concentration, while increasing temperature can preferentially induce the formation of arene rings and reduce nonprotonated carbons resonating near 90 ppm.

4.10. Homogeneity on the 5-nm scale

In electron micrographs, hydrochar usually reveals a characteristic spherical-particle structure [9,10]. Detailed features have been interpreted in terms of an aromatic–aliphatic core–shell model with a shell thickness ≥10 nm [9,10]. The 2D ^{13}C exchange spectra of hydrochar indicate compositional homogeneity on the 5 nm scale and thus do not support models with a large-scale compositional domain structure. ^{13}C magnetization from alkyl segments or ketones equilibrates with that of aromatic rings within 1 s. The observed homogeneity justifies the development (see below) of representative structural models containing a few hundred carbon atoms; if domains were observed, each domain would have to be modeled separately.

4.11. Development of representative structural models

The 1D and 2D NMR experiments with spectral editing presented here have identified many functional groups and their proximities to other structural fragments. These include monophenols and *ortho*-diphenols, furans with nonprotonated Cα, e.g., linked to alkyl segments, protonated furan Cβ bonded to nonprotonated Cα and Cβ, arenes linked to alkyls, arene CH-C_{np} near C=O and aromatic C-O, C=O linking arenes with arenes and with alkyls, etc. In addition, levulinic acid or fragments of closely related structures are present in glucose hydrochar, in particular when synthesized at low temperature [26].

On the basis of these components, we have constructed various related model structures that are consistent with the elemental composition from combustion analysis and calculated the chemical shifts for all the carbons in the structure, using the ACD/NMR Predictor software. From the chemical shifts, simulated spectra were generated, with realistic line broadening, and compared with the experimental quantitative ^{13}C spectra [3,4]. Based on the degree of disagreement or similarity, we can rule out many models and identify one or a few good representations of a hydrothermal carbon sample. The uncertainty in the chemical shift predictions that the software provides (typically ±8 ppm) roughly matches the Gaussian line broadening applied to the simulated spectra.

Fig. 9 shows a structural model of ^{13}CGlc-1h-180-HA whose elemental composition matches the data from combustion analysis and corresponding simulated ^{13}C NMR spectra without and with dipolar dephasing. The corresponding analysis for ^{13}CGlc-5h-280-NA is shown in Fig. 10. The models contain phenols (marked red), furans (blue), an arene ring (green) and the appropriate amounts of ketone, alkyl CH_2, CH, OCH, and OC_qO linkages to match the experimental spectra. A levulinic acid molecule is also included with ^{13}CGlc-1h-180-HA. The sub-spectra of furan rings (dashed blue lines) and phenols plus arenes (dash-dotted red lines) are included in parts b) and c) of Fig. 9.

While various fragments could be moved around within the model without greatly altering the agreement between simulated and experimental spectra, the relative abundances of different moieties are constrained by the overall line shape in the quantitative spectrum. This includes the ratio of furan to arene (including phenol) rings, which is 7:6 in the model for ^{13}CGlc-1h-180-HA, corresponding to a 28:36 carbon ratio; thus, carbons in phenol rings are slightly more abundant than those in furan rings, which contradicts earlier assignments [26] made without the use of the HOPS NMR technique to disambiguate furan from phenol. The model also shows that at this low synthesis temperature, most arene C is part of phenol rings; there is more than one phenol OH per arene ring, on average.

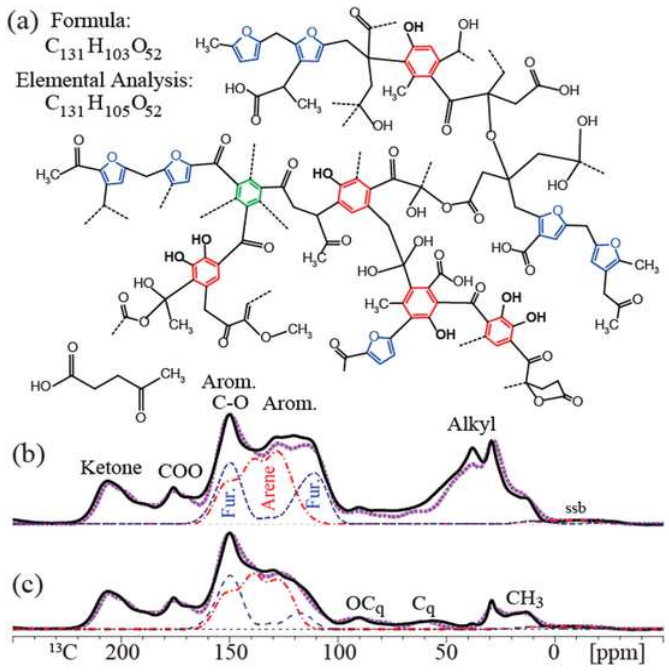

Fig. 9. (a) Representative structural model of ^{13}CGlc-1h-180-HA, whose formula matches elemental composition from combustion analysis (upper left corner), with phenol rings in red and furan rings in blue. Dashed lines are bonds to units outside the structure shown here. (b, c) Corresponding simulated spectra of (b) all carbons and (c) nonprotonated C and (with reduced intensity) CH_3. Experimental spectra: solid black lines; simulations: thick dashed purple lines. Red dash-dotted lines: Subspectra of phenol and other arene rings; blue dashed lines: subspectra of furans in the model. Dashed lines in the model indicate bonds connecting to other, similar ~130-carbon units. The model also incorporated levulinic acid as shown. ssb: spinning sidebands.

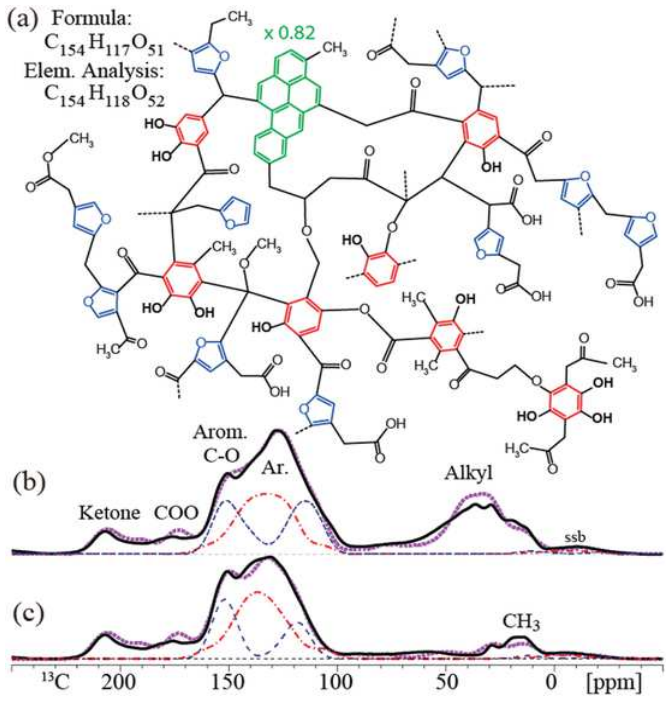

Fig. 10. (a) Representative structural model of ^{13}CGlc-5h-280-NA, with phenol rings in red and furan rings in blue. Dashed lines are bonds to units outside the structure shown here. (b, c) Corresponding simulated spectra of (b) all carbons and (c) nonprotonated C and CH_3. The contribution of the fused-ring system (green) was scaled by a factor of 0.82 relative to the matrix. Experimental spectra: solid black lines; simulations: thick dashed purple lines. Red dash-dotted lines: Sub-spectra of phenols; blue dashed lines: sub-spectra of furans in the model.

The model proposed for ^{13}CGlc-5h-280-NA, also consistent with elemental analysis, in Fig. 10 includes a cluster of fused arene rings that contribute 11 % of all carbons. The ratio of furan to phenol rings (including several diphenols) is 10:7, corresponding to a 40:56 carbon ratio; thus, carbons in phenol rings are again slightly more abundant than carbons in furans.

4.12. Test of hydrochar models in the literature

The quantitative ^{13}C NMR spectra obtained here and the simulation of spectra from structural models also enable tests of hydrochar models previously proposed in the literature. Fig. 11 presents comparisons between spectra simulated for three highly cited hydrochar models [10,16,25] and our quantitative measured spectra. For the arene-rich models, the comparison is made with arene-rich hydrochar produced at 280 °C, and for the furan-rich model with hydrochar synthesized at the lower temperature of 180 °C. The converse comparisons are shown in Fig. S16, which also displays the complete model structures that were too large to be included in Fig. 11.

Unlike the newly proposed models in Figs. 9 and 10, each of the literature models in Fig. 11 contains glaring discrepancies with experiment that relate to well-known major chemical shift trends. Any model of glucose hydrochar must contain abundant aromatic C-O to match the strong peak near 150 ppm; the models in Figs. 11a and b have too little. All three models lack ketones bonded to two sp^3-hybridized carbons producing the peak near 208 ppm, *ortho*-diphenols contributing strongly near 143 ppm, or quaternary carbons revealed by dipolar dephasing. One must conclude that none of the fits is satisfactory, meaning that this analysis rules out all three models, both for low- and high-temperature hydrochars.

Beyond the discrepancies apparent in the comparison of the 1D spectra, the three models also lack features that can only be resolved by spectral editing of overlapping peaks from different types of structures, like phenols from furans. For instance, many of the phenolic ethers in the model of Fig. 11a would have to be replaced by phenols terminated by the OH groups detected by HOPS NMR.

The structures shown in Figs. 9 and 10 are therefore a clear advance compared to the previous state of knowledge, as shown in Fig. 11. While some superficial similarities exist, the new structures differ from those previously reported in the literature in several key ways. For instance, none of the previous models accurately captures the relative importance of furans and arenes in hydrochar. While furans and arenes are both aromatic, they are expected to interact differently with adsorbates [59] and to have different thermal and oxidative stabilities [23,59]. Diels-Alder reactions are a potential way to modify hydrochars, and here furans and arenes are expected to behave entirely differently from one another [60]. Similarly, the level of aromatic fusion – which had been a source of disparity in the literature – is now clarified. Un-fused structures have been found for low-temperature hydrochar, not unexpectedly, whereas high-temperature hydrochar consists of a hybrid structure with unfused and some fused aromatic portions. Aromatic fusion may play a role in adsorption and plays a determining role in environmental stability [61].

Finally, totally new features have been revealed by the current analysis that were completely missing from previously proposed hydrochar structures, including *ortho*-diphenols, aldehydes, and alkene-bearing groups. Non-phenolic arene compounds are now thought to occur rarely in hydrochar made at low temperature. Further, oxygen-containing functional groups such as *ortho*-diphenols are expected to play a key role in adsorption phenomena; the identification of specific groups provides clear targets for future simulation and designer synthesis studies. Alkenes and aldehydes provide reactive targets for hydrochar functionalization, a technique which can be useful for conferring specific properties to hydrochar and other carbon materials [62,63]. Whereas previous work in these areas could be guided by intuition and performed using trial and error techniques, the new structures – and methods – reported here permit for rational design of hydrochars, an advance that can reasonably be expected to aid future efforts in this area.

5. Conclusions

The chemical structures of nine ^{13}C-enriched glucose hydrochars prepared at various temperatures, acidities, and synthesis times were investigated by advanced solid-state ^{13}C NMR. All hydrochars studied share a base structure consisting of phenols, furans, ketones, and non-polar alkyl CH_2 and CH. Comprehensive spectral editing, also of 2D NMR spectra, revealed specific structural features such as *ortho*-diphenols, ketone-stabilized enols, methylene-linked furans and C=O, and OC_q likely in a cyclic ester. The simultaneous presence of both furans and phenols, including *ortho*-diphenols, which are difficult to distinguish without spectral editing, was proved through hydroxyl-proton selection combined with 2D NMR. Processing time beyond 1 h did not change the NMR spectra significantly. At the lower temperatures (180 and 200 °C), some alkenes form, but these are not observed at higher synthesis temperature (280 °C), where instead arene structures become more abundant and begin to fuse into polycyclic aromatic hydrocarbon subunits. The previously proposed core–shell model of hydrochar microspheres is not supported by NMR with ^{13}C spin diffusion. Comprehensive representative structural models conveniently display the structural information obtained from the advanced NMR experiments, while many aspects of models previously proposed in the literature can be ruled out. The detailed models provided here are expected to permit rational design of hydrochars for specific purposes.

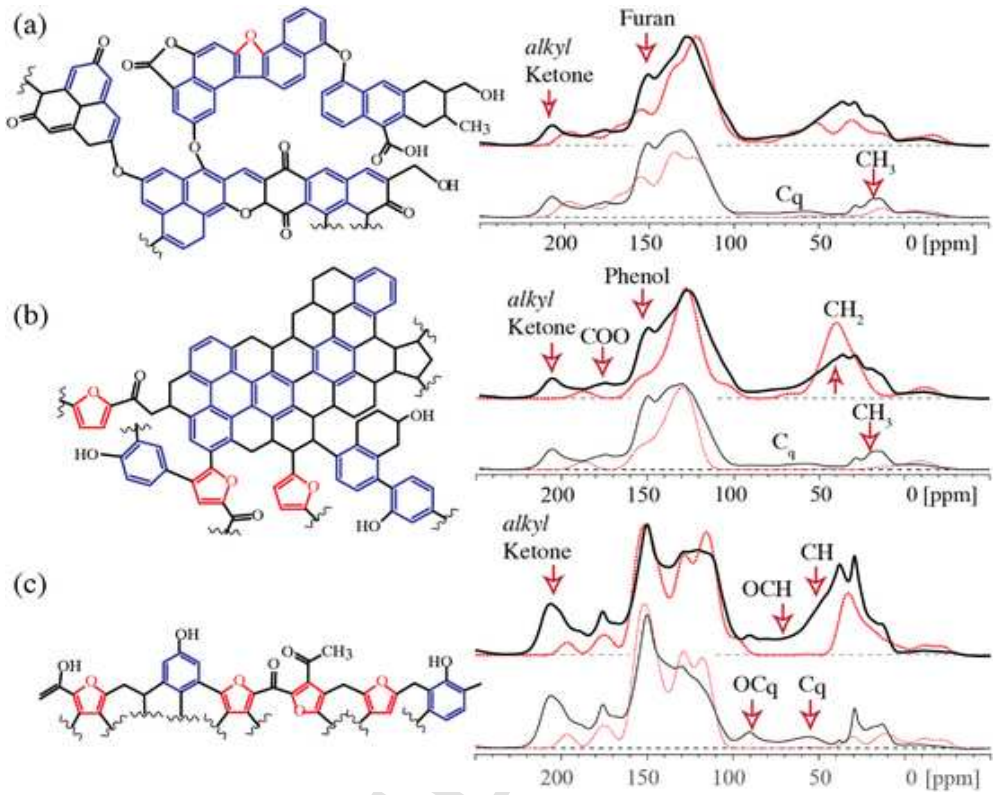

Fig. 11. Comparison of quantitative ^{13}C NMR spectra of hydrochars (in black; thin lines: after dipolar dephasing) with spectra predicted (in red, dashed) based on models from the literature, in (a) ref. [10], (b) ref. [25], and (c) ref. [16]. Characteristic parts of each model are shown. The full model structures used in the simulations are presented in Fig. S16. For the arene-rich models in (a) and (b), comparison is made with high-temperature, ^{13}CGlc-5h-280-NA, hydrochar, while the furan-rich model in (c) is compared with low-temperature, ^{13}CGlc-1h-180-HA, hydrochar. Pronounced discrepancies are marked by arrows. The discrepancies in the converse comparisons are even larger, see Fig. S16.

Author contributions

Shichen Yuan: Writing - original draft; Investigation; Formal analysis; Software; Visualization. Avery Brown: Investigation, Data curation; Investigation; Methodology; Writing - review & editing. Zhaoxi Zheng: Formal analysis; Visualization; Writing - review & editing. Robert L. Johnson: Conceptualization; Investigation; Writing - review & editing. Karen Agro: Writing: review & editing; Formal analysis. Andrea Kruse: Resources; Writing - review & editing; Supervision. Michael T. Timko: Writing - review & editing; Conceptualization; Project administration. Klaus. Schmidt-Rohr: Conceptualization; Funding Acquisition; Investigation; Methodology; Project administration; Resources; Supervision; Validation; Writing – original draft, review & editing.

Declaration of competing interest

The authors declare that they have no known competing financial interests or personal relationships that could have appeared to influence the work reported in this paper.

6. Acknowledgements

This work was partially supported by a collaborative NSF2026/EAGER grant CBET 2032590. The solid-state NMR spectrometer used in this work was funded by the NSF MRI program (Award No. 1726346).

Data availability

Data will be made available on request.

Appendix A. Supplementary data

Supplementary data to this article can be found online at https://doi.org/10.1016/j.ssnmr.2024.101973.

References

[1] B. Hu, K. Wang, L. Wu, S.H. Yu, M. Antonietti, M.M. Titirici, Engineering carbon materials from the hydrothermal carbonization process of biomass, Adv. Mater. 22 (2010) 813–828. http://10.1002/adma.200902812.
[2] J. Fang, L. Zhan, Y.S. Ok, B. Gao, Minireview of potential applications of hydrochar derived from hydrothermal carbonization of biomass, J. Ind. Eng. Chem. 57 (2018) 15–21. http://10.1016/j.jiec.2017.08.026.
[3] H.N. Pham, A.E. Anderson, R.L. Johnson, K. Schmidt-Rohr, A.K. Datye, Improved hydrothermal stability of mesoporous oxides for reactions in the aqueous phase, Angew. Chem. 124 (2012) 13340–13344. http://10.1002/ange.201206675.
[4] J.M. Anderson, R.L. Johnson, K. Schmidt-Rohr, B.H. Shanks, Solid state NMR study of chemical structure and hydrothermal deactivation of moderate-temperature carbon materials with acidic SO_3H sites, Carbon 74 (2014) 333–345. http://10.1016/j.carbon.2014.03.041.
[5] Y. Wang, P. Guerra, A. Zaker, A.R. Maag, G.A. Tompsett, L.J. Smith, X. Huang, J.Q. Bond, M.T. Timko, Strategies for extending zeolite stability in supercritical water using thermally stable coatings, ACS Catal. 10 (2020) 6623–6634. http://10.1021/acscatal.0c01722.
[6] T. Wang, Y. Zhai, Y. Zhu, C. Li, G. Zeng, A review of the hydrothermal carbonization of biomass waste for hydrochar formation: process conditions, fundamentals, and physicochemical properties, Renew. Sustain. Energy Rev. 90 (2018) 223–247. http://10.1016/j.rser.2018.03.071.
[7] Y. Gao, X. Wang, J. Wang, X. Li, J. Cheng, H. Yang, H. Chen, Effect of residence time on chemical and structural properties of hydrochar obtained by hydrothermal carbonization of water hyacinth, Energy 58 (2013) 376–383. http://10.1016/j.energy.2013.06.023.
[8] C. Peng, Y. Zhai, Y. Zhu, B. Xu, T. Wang, C. Li, G. Zeng, Production of char from sewage sludge employing hydrothermal carbonization: char properties, combustion behavior and thermal characteristics, Fuel 176 (2016) 110–118. http://10.1016/j.fuel.2016.02.068.

[9] Y. Shin, L.-Q. Wang, I.-T. Bae, B.W. Arey, G.J. Exarhos, Hydrothermal syntheses of colloidal carbon spheres from cyclodextrins, J. Phys. Chem. C 112 (2008) 14236–14240. http://10.1021/jp801343y.

[10] M. Sevilla, A.B. Fuertes, The production of carbon materials by hydrothermal carbonization of cellulose, Carbon 47 (2009) 2281–2289. http://10.1016/j.carbon.2009.04.026.

[11] N. Baccile, C. Falco, M.-M. Titirici, Characterization of biomass and its derived char using ^{13}C-solid state nuclear magnetic resonance, Green Chem. 16 (2014) 4839–4869. http://10.1039/c3gc42570c.

[12] I. Bargmann, M.C. Rillig, A. Kruse, J.M. Greef, M. Kücke, Effects of hydrochar application on the dynamics of soluble nitrogen in soils and on plant availability, J. Plant Nutr. Soil Sci. 177 (2014) 48–58. http://10.1002/jpln.201300069.

[13] D.P. Bezerra, R.S. Oliveira, R.S. Vieira, C.L. Cavalcante, D. Azevedo, Adsorption of CO_2 on nitrogen-enriched activated carbon and zeolite 13X, Adsorption 17 (2011) 235–246. http://10.1007/s10450-011-9320-z.

[14] Y. Shi, T. Zhang, H. Ren, A. Kruse, R. Cui, Polyethylene imine modified hydrochar adsorption for chromium (VI) and nickel (II) removal from aqueous solution, Bioresour. Technol. 247 (2018) 370–379. http://10.1016/j.biortech.2017.09.107.

[15] F. Gao, G. Shao, J. Qu, S. Lv, Y. Li, M. Wu, Tailoring of porous and nitrogen-rich carbons derived from hydrochar for high-performance supercapacitor electrodes, Electrochim. Acta 155 (2015) 201–208. http://10.1016/j.electacta.2014.12.069.

[16] K.G. Latham, M.I. Simone, W.M. Dose, J.A. Allen, S.W. Donne, Synchrotron based NEXAFS study on nitrogen doped hydrothermal carbon: insights into surface functionalities and formation mechanisms, Carbon 114 (2017) 566–578. http://10.1016/j.carbon.2016.12.057.

[17] K. Jurkiewicz, L. Hawelek, K. Balin, J. Szade, F.L. Braghiroli, V. Fierro, A. Celzard, A. Burian, Conversion of natural tannin to hydrothermal and graphene-like carbons studied by wide-angle X-ray scattering, J. Phys. Chem. A 119 (2015) 8692–8701. http://10.1021/acs.jpca.5b02407.

[18] J.L. Figueiredo, M.F.R. Pereira, M.M.A. Freitas, J.J.M. Órfão, Modification of the surface chemistry of activated carbons, Carbon 37 (1999) 1379–1389. http://10.1016/s0008-6223(98)00333-9.

[19] R. Haerle, E. Riedo, A. Pasquarello, A. Baldereschi, Sp^2/sp^3 hybridization ratio in amorphous carbon from C1s core-level shifts: X-ray photoelectron spectroscopy and first-principles calculation, Phys. Rev. B 65 (2001). http://10.1103/PhysRevB.65.045101.

[20] K.G. Latham, G. Jambu, S.D. Joseph, S.W. Donne, Nitrogen doping of hydrochars produced hydrothermal treatment of sucrose in H_2O, H_2SO_4, and NaOH, ACS Sustain. Chem. Eng. 2 (2014) 755–764. http://10.1021/sc4004339.

[21] J. Landoulsi, M.J. Genet, S. Fleith, Y. Touré, I. Liascukiene, C. Méthivier, P.G. Rouxhet, Organic adlayer on inorganic materials: XPS analysis selectivity to cope with adventitious contamination, Appl. Surf. Sci. 383 (2016) 71–83. http://10.1016/j.apsusc.2016.04.147.

[22] M.A. Pimenta, G. Dresselhaus, M.S. Dresselhaus, L.G. Cancado, A. Jorio, R. Saito, Studying disorder in graphite-based systems by Raman spectroscopy, Phys. Chem. Chem. Phys. 9 (2007) 1276–1291. http://10.1039/b613962k.

[23] A.B. Brown, G.A. Tompsett, B. Partopour, N.A. Deskins, M.T. Timko, Hydrochar structural determination from artifact-free Raman analysis, Carbon 167 (2020) 378–387. http://10.1016/j.carbon.2020.06.021.

[24] A.B. Brown, B.J. McKeogh, G.A. Tompsett, R. Lewis, N.A. Deskins, M.T. Timko, Structural analysis of hydrothermal char and its models by density functional theory simulation of vibrational spectroscopy, Carbon 125 (2017) 614–629. http://10.1016/j.carbon.2017.09.051.

[25] A. Chuntanapum, Y. Matsumura, Formation of tarry material from 5-HMF in subcritical and supercritical water, Ind. Eng. Chem. Res. 48 (2009) 9837–9846. http://10.1021/ie900423g.

[26] N. Baccile, G. Laurent, F. Babonneau, F. Fayon, M.-M. Titirici, M. Antonietti, Structural characterization of hydrothermal carbon spheres by advanced solid-state MAS ^{13}C NMR investigations, J. Phys. Chem. C 113 (2009) 9644–9654. http://10.1021/jp901582x.

[27] K. Schmidt-Rohr, J.D. Mao, Efficient CH-group selection and identification in ^{13}C solid-state NMR by dipolar DEPT and ^{1}H chemical-shift filtering, J. Am. Chem. Soc. 124 (2002) 13938–13948. http://10.1021/ja027362m.

[28] J.D. Mao, K. Schmidt-Rohr, Separation of aromatic-carbon ^{13}C NMR signals from di-oxygenated alkyl bands by a chemical-shift-anisotropy filter, Solid State Nucl. Magn. Reson. 26 (2004) 36–45. http://10.1016/j.ssnmr.2003.09.003.

[29] J.D. Mao, K. Schmidt-Rohr, Methylene spectral editing in solid-state ^{13}C NMR by three-spin coherence selection, J. Magn. Reson. 176 (2005) 1–6. http://10.1016/j.jmr.2005.04.016.

[30] P. Duan, K. Schmidt-Rohr, Quick, selective NMR spectra of C-OH moieties in ^{13}C-enriched solids, J. Magn. Reson. 301 (2019) 80–84. http://10.1016/j.jmr.2019.02.007.

[31] R.L. Johnson, J.M. Anderson, B.H. Shanks, X. Fang, M. Hong, K. Schmidt-Rohr, Spectrally edited 2D ^{13}C-^{13}C NMR spectra without diagonal ridge for characterizing ^{13}C-enriched low-temperature carbon materials, J. Magn. Reson. 234 (2013) 112–124. http://10.1016/j.jmr.2013.06.006.

[32] D. Jung, M. Zimmermann, A. Kruse, Hydrothermal carbonization of fructose: growth mechanism and kinetic model, ACS Sustain. Chem. Eng. 6 (2018) 13877–13887. http://10.1021/acssuschemeng.8b02118.

[33] A.E. Bennett, C.M. Rienstra, M. Auger, K.V. Lakshmi, R.G. Griffin, Heteronuclear decoupling in rotating solids, J. Chem. Phys. 103 (1995) 6951–6958. http://10.1063/1.470372.

[34] E.L. Hahn, Spin echoes, Phys. Rev. 80 (1950) 580–594. http://10.1103/PhysRev.80.580.

[35] W.T. Dixon, J. Schaefer, M.D. Sefcik, E.O. Stejskal, R.A. McKay, Total suppression of sidebands in CPMAS C-13 NMR, J. Magn. Reson. 49 (1982) (1969) 341–345. http://10.1016/0022-2364(82)90199-8.

[36] B.M. Fung, A.K. Khitrin, K. Ermolaev, An improved broadband decoupling sequence for liquid crystals and solids, J. Magn. Reson. 142 (2000) 97–101. http://10.1006/jmre.1999.1896.

[37] J.D. Mao, K. Schmidt-Rohr, Accurate quantification of aromaticity and nonprotonated aromatic carbon fraction in natural organic matter by ^{13}C solid-state nuclear magnetic resonance, Environ. Sci. Technol. 38 (2004) 2680–2684. http://10.1021/es034770x.

[38] P. Caravatti, L. Braunschweiler, R.R. Ernst, Heteronuclear correlation spectroscopy in rotating solids, Chem. Phys. Lett. 100 (1983) 305–310. http://10.1016/0009-2614(83)80276-0.

[39] A. Bielecki, A.C. Kolbert, H.J.M. De Groot, R.G. Griffin, M.H. Levitt, Frequency-switched lee—goldburg sequences in solids, in: W.S. Warren (Ed.), Advances in Magnetic and Optical Resonance, Academic Press, San Diego, 1990, pp. 111–124.

[40] M. Hohwy, C.M. Rienstra, C.P. Jaroniec, R.G. Griffin, Fivefold symmetric homonuclear dipolar recoupling in rotating solids: application to double quantum spectroscopy, J. Chem. Phys. 110 (1999) 7983–7992. http://10.1063/1.478702.

[41] J. Jeener, B.H. Meier, P. Bachmann, R.R. Ernst, Investigation of exchange processes by two-dimensional NMR spectroscopy, J. Chem. Phys. 71 (1979) 4546–4553. http://10.1063/1.438208.

[42] H. Geen, M.H. Levitt, G. Bodenhausen, Preparing initial conditions for rotational resonance in solid state NMR spectroscopy, Chem. Phys. Lett. 200 (1992) 350–356. http://10.1016/0009-2614(92)87002-7.

[43] H. Geen, G. Bodenhausen, Complete sideband suppression in magic angle spinning solid-state nuclear magnetic resonance for arbitrary chemical shift anisotropies, J. Am. Chem. Soc. 115 (1993) 1579–1580. http://10.1021/ja00057a055.

[44] K. Takegoshi, S. Nakamura, T. Terao, ^{13}C–^{1}H dipolar-assisted rotational resonance in magic-angle spinning NMR, Chem. Phys. Lett. 344 (2001) 631–637. http://10.1016/s0009-2614(01)00791-6.

[45] ACD/Structure Elucidator, Version 12.01, Advanced Chemistry Development, Inc., Toronto, ON, Canada, 2014.

[46] H.S. Kambo, A. Dutta, A comparative review of biochar and hydrochar in terms of production, physico-chemical properties and applications, Renew. Sustain. Energy Rev. 45 (2015) 359–378. http://10.1016/j.rser.2015.01.050.

[47] J. Wu, T. Wang, Y. Zhang, W.-P. Pan, The distribution of Pb (II)/Cd (II) adsorption mechanisms on biochars from aqueous solution: considering the increased oxygen functional groups by HCl treatment, Bioresour. Technol. 291 (2019). 121859. http://10.1016/j.biortech.2019.121859.

[48] M. Uchimiya, L.H. Wartelle, K.T. Klasson, C.A. Fortier, I.M. Lima, Influence of pyrolysis temperature on biochar property and function as a heavy metal sorbent in soil, J. Agric. Food Chem. 59 (2011) 2501–2510. http://10.1021/jf104206c.

[49] S.K.R. Patil, C.R.F. Lund, Formation and growth of humins via aldol addition and condensation during acid-catalyzed conversion of 5-hydroxymethylfurfural, Energy & Fuels 25 (2011) 4745–4755. http://10.1021/ef2010157.

[50] Y. Kida, C.A. Class, A.J. Concepcion, M.T. Timko, W.H. Green, Combining experiment and theory to elucidate the role of supercritical water in sulfide decomposition, Phys. Chem. Chem. Phys. 16 (2014) 9220–9228. http://10.1039/c4cp00711e.

[51] E. Dumitriu, V. Hulea, I. Fechete, A. Auroux, J.-F. Lacaze, C. Guimon, The aldol condensation of lower aldehydes over MFI zeolites with different acidic properties, Microporous Mesoporous Mat 43 (2001) 341–359. http://10.1016/S1387-1811(01)00265-7.

[52] N. Shi, Q. Liu, X. He, G. Wang, N. Chen, J. Peng, L. Ma, Molecular structure and formation mechanism of hydrochar from hydrothermal carbonization of carbohydrates, Energy & Fuels 33 (2019) 9904–9915. http://10.1021/acs.energyfuels.9b02174.

[53] Q. He, Y. Yu, J. Wang, X. Suo, Y. Liu, Kinetic study of the hydrothermal carbonization reaction of glucose and its product structures, Ind. Eng. Chem. Res. 60 (2021) 4552–4561. http://10.1021/acs.iecr.0c06280.

[54] B.S. Matsuura, S. Huss, Z. Zheng, S. Yuan, T. Wang, B. Chen, J.V. Badding, D. Trauner, E. Elacqua, A.C.T. van Duin, V.H. Crespi, K. Schmidt-Rohr, Perfect and defective $^{13}C_4$-furan-derived nanothreads from modest-pressure synthesis analyzed by ^{13}C NMR, J. Am. Chem. Soc. (2021). http://10.1021/jacs.1c03671.

[55] K.G. Latham, A. Rawal, J.M. Hook, S.W. Donne, Molecular structures driving pseudo-capacitance in hydrothermal nanostructured carbons, RSC Adv. 6 (2016) 12964–12976. http://10.1039/c5ra26136h.

[56] M. Principe, R. Martínez, P. Ortiz, J. Rieumont, The polymerization of furfuryl alcohol with p-toluenesulfonic acid: photocross-linkeable feature of the polymer, Polímeros 10 (2000) 8–14. http://10.1590/s0104-14282000000100004.

[57] G. Tondi, N. Cefarin, T. Sepperer, F. D'Amico, R.J.F. Berger, M. Musso, G. Birarda, A. Reyer, T. Schnabel, L. Vaccari, Understanding the polymerization of polyfurfuryl alcohol: ring opening and diels-alder reactions, Polymers 11 (2019). http://10.3390/polym11122126.

[58] C.L. Burket, R. Rajagopalan, A.P. Marencic, K. Dronvajjala, H.C. Foley, Genesis of porosity in polyfurfuryl alcohol derived nanoporous carbon, Carbon 44 (2006) 2957–2963. http://10.1016/j.carbon.2006.05.029.

[59] L. Delahaye, J.T. Hobson, M.P. Rando, B. Sweeney, A.B. Brown, G.A. Tompsett, A. Ates, N.A. Deskins, M.T. Timko, Experimental and computational evaluation of heavy metal cation adsorption for molecular design of hydrothermal char, Energies 13 (2020) 4203. http://10.3390/en13164203.

[60] O.T. Dyan, G.I. Borodkin, P.A. Zaikin, The Diels–Alder reaction for the synthesis of polycyclic aromatic compounds, Eur. J. Org. Chem. 2019 (2019) 7271–7306. http://10.1002/ejoc.201901254.

[61] C.-H. Liu, W. Chu, H. Li, S.A. Boyd, B.J. Teppen, J. Mao, J. Lehmann, W. Zhang,

Quantification and characterization of dissolved organic carbon from biochars, Geoderma 335 (2019) 161–169. http://10.1016/j.geoderma.2018.08.019.
[62] T. Chhabra, P. Dwivedi, V. Krishnan, Acid functionalized hydrochar as heterogeneous catalysts for solventless synthesis of biofuel precursors, Green Chem. 24 (2022) 898–910. http://10.1039/d1gc03330a.
[63] H.N. Tran, F.-C. Huang, C.-K. Lee, H.-P. Chao, Activated carbon derived from spherical hydrochar functionalized with triethylenetetramine: synthesis, characterizations, and adsorption application, Green Process. Synth. 6 (2017) 565–576. http://10.1515/gps-2016-0178.